J. Appl. Comput. Mech., 11(4) (2025) 975-990
DOI: 10.22055/jacm.2024.47920.4842

ISSN: 2383-4536
jacm.scu.ac.ir

Shahid Chamran University of Ahvaz

Journal of Applied and Computational Mechanics

Research Paper

Non-uniform Porosity Distribution on a Hollow Cylinder with Thermo-magnetic Mechanical Loading

Rania M. Tantawy[1], Mohammed A. Alghamdi[2], Ashraf M. Zenkour[2,3]

[1] Department of Mathematics, Faculty of Science, Damietta University, P.O. Box 34517, Egypt, Email: rania_eltantwy@yahoo.com

[2] Department of Mathematics, Faculty of Science, King Abdulaziz University, P.O. Box 80203, Jeddah 21589, Saudi Arabia, Email: mamalgamdi@kau.edu.sa

[3] Department of Mathematics, Faculty of Science, Kafrelsheikh University, Kafrelsheikh 33516, Egypt, Email: zenkour@sci.kfs.edu.eg, zenkour@kau.edu.sa

Received September 14 2024; Revised October 24 2024; Accepted for publication December 15 2024.
Corresponding author: R.M. Tantawy (rania_eltantwy@yahoo.com)

Abstract. Currently, with the tremendous development in manufacturing composite materials, porous functionally graded materials have attracted many engineering, thermal, and electrical studies and applications on porous structures as most recent applications in functionally graded (FG) materials. In this study, semi-analytical solutions are investigated for perfect and porous FG hollow cylinders influenced by magnetic, and thermo-mechanical loads. Porosities with random distribution on the cylinder are considered. Magneto-thermo elastic characteristic of porous FG cylinder is substantive by modulated power law for even and uneven distributions of porosity in a radial direction of a porous hollow cylinder. The contribution of the present paper is demonstrated in providing complete elastic solutions for porous FG cylinders by considering perfect, even, and uneven distribution. Also, the validation of the grading index and porosity factor on the porous cylinder is reported for two different cases of boundary conditions. All of the two cases are studied in detail and the results of comparison between perfect and porous material are tabulated and discussed. The conclusion of this study should assist with developing mechanical engineering applications.

Keywords: Porosity; Hollow cylinder; Magnetic field; Temperature; Semi-analytical solution; Functionally graded.

1. Introduction

Industrial development day by day enhances the properties of materials. Traditional pure materials such as alloys and metals are no longer sufficient to meet the basic requirements suitable for many industrial applications. Therefore, it was necessary to produce novel substances [1] with graduate characteristics to meet the requirements of the industrial revolution, which led to the beginning of the birth of graded materials. Most industrial applications in the fields of construction, space, mobile phones, and cars require materials with gradually changing properties [2] in structure and composition over the entire material in certain directions, and this is what characterizes materials with gradual properties [3] so they can be applied in many modern industrial and engineering applications [4].

FGM has aroused great interest in mechanical and thermal problems for many complex mathematical and engineering models. Xie *et al.* [5] obtained an accurate solution for FG pressure vessels. Saadatfar and Zarandi [6] discuss the effectiveness of mechanical loading and angular acceleration on rotating tapered disks with gradual exponential law. Allam [7] illustrated the semi-analytical solution for the full elastic solution of hygrothermal and electric load in solid and annular cylinders. Allam [8] presented various cases of exponentially graded spheres affected by different types of loads. Thanh [9] studied expanding the ES-MITC3 element enforced by mechanical loads for the buckling study of FGM tapered plate. Saadatfar and Zarandi [10] used the shooting technique and Runge-Kutta method to present the effect of angular acceleration on mechanistic resistance of piezoelectric exponentially graduate material rotary annular sheet for tapered thickness in a static magnetic medium. Sharma *et al.* [11] interpreted the finite element technique to get the solution of thermoelastic analysis of rotary FGM.

FG porous substances have many advantages and properties that provide design freedom and reduce the density and weight of the final structure. It provides better dent capacity [12, 13] and more structural rigidity [14]. Porous materials have less weight and greater surface density while providing more flexibility to the structures [15]. With mechanical properties allowing advanced functionality. Thus, porous functionally graded materials are a better choice while controlling the porosity distribution to develop multi-functional, lower-weight structures. Cardboard, paper, sponges, stones, cork, and untreated wood are some examples of porous substances. Many scientific papers have been prepared and discussed recently to study porosity and the attitude of structures on the impact of porosity on functionally graded materials. Tantawy and Zenkour [16] present the hygrothermal effect on the porous functionally graded sphere under thermomechanical loads. Wattanasakulpong and Ungbhakorn [17] studied vibration in FGM rays with various porosity distributions by differential processing technique. A mathematical model of hollow

Published online: December 19 2024

structures (sphere-cylinder) was studied using a semi-analytical method in a humid thermal medium while presenting the impact of magnetic medium and porosity on the structure made of an isotropic material by Tantawy [18]. Babaei *et al.* [19] introduced survey research about porosity in FGM structures. Nathi [20] Using the high shear deformation notion, he was able to resolve the buckling in two dimensions of porous FGM beams. Tantawy and Zenkour [21] concluded a thermomechanical solution for FG viscoelastic exponentially tapered disk. Using the differential quadrature technique and modified couple stress theory, Li *et al.* [22] were able to provide an analysis of FG axial microtubules. Li *et al.* [23] offered a survey on the dynamics of a sandwich of an FGM containing a porous core. Tantawy and Zenkour [24] discussed thermomagnetic, rotation, thickness variation, and porosity influence on FG disks.

Many researchers have been interested in studying porosity distributions, especially the even and uneven distribution of porosity. Ebrahimi *et al.* [25] presented a paper for even and uneven distribution forms. Akbas [26] illustrated the vibration of FG beams with thermal loading by even and uneven porosity description. Tantawy and Zenkour [27] discussed even and uneven distribution of porosity on rotary FG tapered disks with electro-magneto-thermo-mechanical forces. By even and uneven porosity distribution Barati and Shahverdi [28] illustrated hygro-aero thermal stability of FG board.

The current work is concerned with studying non-uniform porosity distribution. The distribution of even and uneven porosity on a functionally graded hollow cylinder was studied and presented. The cylinder is exposed to a collection of thermal, mechanical, and electromagnetic loading affecting the cylinder radii. Physical and thermal parameters of the cylinder change in the orientation of the radii. Using Maxwell's laws and Lorentz force, we were able to acquire the solution of the electrostatic equation. The temperature equation and differential equilibrium equations are solved by employing a semi-analytical technique. Several parameters were studied for two different boundary conditions to study the influence of the inhomogeneity coefficient and porosity factor for a porous and perfect cylinder. The numerical results are tabulated for future comparisons and a comparison between the porous (even-uneven) case and the perfect case of the cylinder is presented for two boundary conditions in detail.

2. Description of the Porous Cylinder Structure

A long, symmetrical porous hollow cylinder rotating around a fixed axis made of FGM. The cylinder is made of a substance with good electrical conductivity. The cylinder is exposed to thermal influence and mechanical load and is put in a static magnetic domain. The geometric dimensions of the cylinder are internal radius a made of PZT-4 and external radius b made of Cadmium Selenide. The cylinder's thermal and physical parameters graded from PZT on the internal surface to Cadmium Selenide on the external surface. All cylinder parameters are compiled in Table 1 [29, 30]. To complete the geometric description, we use cylindrical coordinates (r, θ, z) to describe the geometric structure of the cylinder.

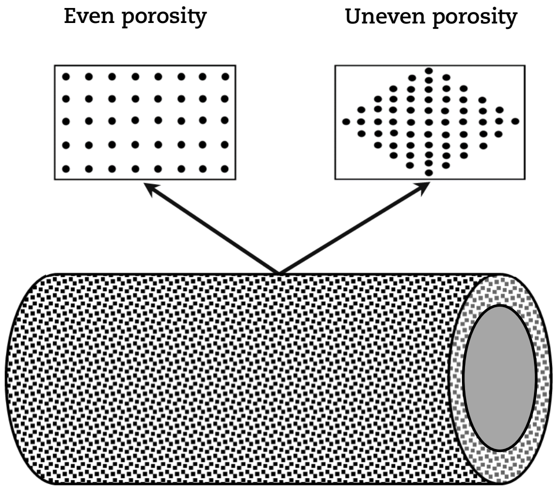

Fig. 1. Organization porosity distribution on the cylinder.

Table 1. Numerical values of the cylinder's thermal and physical parameters.

PZT-4 [29]	Cadmium selenide [30]
$c_{rr}^{(a)} = 115 \times 10^9$ (Pa)	$c_{rr}^{(b)} = 83.6 \times 10^9$ (Pa)
$c_{r\theta}^{(a)} = 74.3 \times 10^9$ (Pa)	$c_{r\theta}^{(b)} = 39.3 \times 10^9$ (Pa)
$c_{\theta\varphi}^{(a)} = 77.8 \times 10^9$ (Pa)	$c_{\theta\varphi}^{(b)} = 45.2 \times 10^9$ (Pa)
$c_{\theta\theta}^{(a)} = 139 \times 10^9$ (Pa)	$c_{\theta\theta}^{(b)} = 74.1 \times 10^9$ (Pa)
$e_{rr}^{(a)} = 15.1$ (Cm^{-2})	$e_{rr}^{(b)} = 0.347$ (Cm^{-2})
$e_{r\theta}^{(a)} = -5.2$ (Cm^{-2})	$e_{r\theta}^{(b)} = 0.16$ (Cm^{-2})
$\varepsilon_{rr}^{(a)} = 3.87 \times 10^{-9}$ $(\mathrm{C^2K^{-1}m^2})$	$\varepsilon_{rr}^{(b)} = 9.03 \times 10^{-11}$ $(\mathrm{C^2K^{-1}m^2})$
$p_{11}^{(a)} = -2.5 \times 10^{-5}$ $(\mathrm{CK^{-1}m^{-2}})$	$p_{11}^{(b)} = -2.94 \times 10^{-6}$ $(\mathrm{CK^{-1}m^{-2}})$
$K_{\mathrm{T}}^{(a)} = 110$ $(\mathrm{WK^{-1}m^{-1}})$	$K_{\mathrm{T}}^{(b)} = 4$ $(\mathrm{WK^{-1}m^{-1}})$
$\alpha_r^{(a)} = 2 \times 10^{-5}$ $(\mathrm{K^{-1}})$	$\alpha_r^{(b)} = 2.458 \times 10^{-6}$ $(\mathrm{K^{-1}})$
$\alpha_\theta^{(a)} = 2 \times 10^{-6}$ $(\mathrm{K^{-1}})$	$\alpha_\theta^{(b)} = 4.396 \times 10^{-6}$ $(\mathrm{K^{-1}})$
$\mu^{(a)} = 4\pi \times 10^{-7} (\mathrm{Hm^{-1}})$	$\mu^{(b)} = 6.15 \times 10^{-5} (\mathrm{Hm^{-1}})$
$\rho^{(a)} = 7500 (\mathrm{kg\ m^{-3}})$	$\rho^{(b)} = 5684 (\mathrm{kg\ m^{-3}})$

3. Porosity Properties with Even and Uneven Formulation

Assuming that the porosity distribution over the cylinder structure is given by three different mathematical relationships. An even distribution relationship and two logarithmic uneven distribution relationships, as in Fig. 1. The parameters and properties of the material graded in the orientation of the radius from the internal surface to the external surface are compatible with a power equation $p(r)$ as shown [31, 32]:

$$p(r)=\begin{cases}(p_b-p_a)(\frac{r-a}{b-a})^n+p_a-\frac{1}{2}\beta(p_b+p_a) & \text{even}\\ (p_b-p_a)(\frac{r-a}{b-a})^n+p_a-\ln(\frac{1}{2}\beta+1)\,(p_b+p_a)\frac{r}{b} & \text{uneven I},\\ (p_b-p_a)(\frac{r-a}{b-a})^n+p_a-\ln(\frac{1}{2}\beta+1)\,(p_b+p_a)(1-\frac{r}{b}) & \text{uneven II}\end{cases} \tag{1}$$

which p_a and p_b are the characteristics of the interior and exterior radii of the cylinder respectively, $n\geq 0$ characterize the grading index, and β is the porosity factor, for porous cylinder $0<\beta<1$ but $\beta=0$ for perfect cylinder.

4. Graded Temperature Equations

The current study is concerned with studying a hollow porous cylinder. Therefore, the Fourier temperature equation was used in one dimension, where the temperature increases in the direction of the radius from the inside to the outside [29, 33,34]:

$$\frac{1}{r}\frac{\mathrm{d}}{\mathrm{d}r}\left(r\;k_T\;\frac{\mathrm{d}T(r)}{\mathrm{d}r}\right)=0, \tag{2}$$

where k_T is the thermal conductivity constants following Eq. (1). Assuming the boundary conditions for temperature distribution over porous cylinder are:

$$T(r)|_{r=a}=T_0,\quad T(r)|_{r=b}=T_1, \tag{3}$$

where T_0 is initial temperature and T_1 the temperature on the exterior radii.

5. Electrodynamics Maxwell's Laws

Assuming that the structure of a porous cylinder is in a static magnetic field and the coefficient of magnetic permeability $\mu(r)$ is graded and follows Eq. (1). Maxwell's equations are four differential equations to describe the interaction and propagation of magnetic and electric fields and how they affect the porous cylinder as follows [35]:

$$\begin{gathered}\underline{J}=\nabla\times\underline{v},\quad \nabla\times\underline{e}=-\mu\frac{\partial v}{\partial t},\quad \nabla.\underline{v}=0,\\ \underline{e}=-\mu(\frac{\partial u}{\partial t}\times\underline{H}),\quad \underline{v}=\nabla\times(\underline{u}\times\underline{H}),\end{gathered} \tag{4}$$

where $\underline{J}$ is the flow density, $\underline{H}$ is a static magnetic field vector, $\underline{v}$ is magnetic field vector and $\underline{e}$ is an electric field vector.

6. Mathematical Governing Equations

The FG porous cylinder is exposed to a combination of forces electric potential $\psi(r)$, thermal conductivity $T(r)$ and mechanical load in a static magnetic field. Thus, the equations of stresses and electrical displacement can be expressed [36, 37,38]:

$$\begin{Bmatrix}\sigma_r\\ \sigma_\theta\\ D_r\end{Bmatrix}=\begin{bmatrix}c_{rr} & c_{r\theta}\\ c_{r\theta} & c_{\theta\theta}\\ e_{rr} & e_{r\theta}\end{bmatrix}\begin{Bmatrix}\frac{\mathrm{d}u}{\mathrm{d}r}\\ \frac{u}{r}\end{Bmatrix}+\begin{Bmatrix}e_{rr}\\ e_{r\theta}\\ -\varepsilon_{rr}\end{Bmatrix}\frac{\mathrm{d}\psi}{\mathrm{d}r}-\begin{Bmatrix}\lambda_r\\ \lambda_\theta\\ -p_{11}\end{Bmatrix}T(r), \tag{5}$$

in which $c_{ij}\ (i,j=r,\theta,z)$ are elastic constants, ε_{rr} is dielectric coefficients, p_{11} is pyroelectric coefficients, $e_{rj}\ (j=r,\theta)$ are piezoelectric parameters, and $\lambda_i\ (i=r,\theta)$ in the form [7]:

$$\lambda_r=c_{rr}\alpha_r+c_{r\theta}\alpha_\theta,\quad \lambda_\theta=c_{r\theta}\alpha_r+c_{\theta\theta}\alpha_\theta, \tag{6}$$

where α_i explain thermal expansion coefficients.

With the movement of the symmetrical porous cylinder around its axis within the static magnetic field, the Lorentz force and inertia forces are generated. Using differential equilibrium equations to study the structure of the porous cylinder with the help of Eqs. (5):

$$\begin{gathered}\frac{\mathrm{d}\sigma_r}{\mathrm{d}r}+\frac{(\sigma_r-\sigma_\theta)}{r}+F_r+F_H=0,\\ F_r=\rho\omega^2 r,\\ F_H=\mu(r)(\underline{J}\times\underline{H})=H^2\frac{\mathrm{d}}{\mathrm{d}r}(\mu(r)\frac{\mathrm{d}u}{\mathrm{d}r}+\mu(r)\frac{u}{r}),\end{gathered} \tag{7}$$

where F_H are Lorentz force, and F_r are inertia force respectively, and the equilibrium electric displacement equation is:

$$\frac{\mathrm{d}}{\mathrm{d}r}(rD_r)=0, \tag{8}$$

in which D_r describes electric displacement.

7. Mathematical Algorithm for the Structure of FG Porous Cylinder

The mathematical algorithm for the solution consists of a few mathematical steps:

- Solve the electrostatic Eq. (8) to obtain the value of the electrical displacement D_r.
- Find the equation of the electric potential function $\frac{\mathrm{d}\psi}{\mathrm{d}r}$.
- Substitute in equilibrium Eq. (7) with the value of $\frac{\mathrm{d}\psi}{\mathrm{d}r}$ and obtain a differential equation for radial displacement u.

- Obtaining the solution of heat Eq. (2), considering k_T gradient according to Eq. (1).
- Solve the differential equilibrium equation in the radial displacement u.
- Obtaining the value of the stresses and electrical potentials of the porous cylinder structure.

We consider two different boundary conditions as follows [39]:

- Case 1: (Free-Free) mechanical pressure and electrical loading on hollow porous cylinder

$$\sigma_r|_{r=a} = -P_1, \quad \sigma_r|_{r=b} = -P_2, \quad \psi(r)|_{r=a} = \psi_1, \quad \psi(r)|_{r=b} = \psi_2. \tag{9}$$

- Case 2: (Fixed-Free) mounted hollow porous cylinder

$$u(r)|_{r=a} = 0, \quad \sigma_r|_{r=b} = -P_2, \quad \psi(r)|_{r=a} = \psi_1, \quad \psi(r)|_{r=b} = \psi_2, \tag{10}$$

in which P_i illustrate forces on inner and outer radii of porous cylinder while ψ_i denote electric potentials in the same radii.

By applying the mathematical algorithm, we first obtain the general solution for the electric displacement:

$$D_r = \frac{A_1}{r}, \tag{11}$$

where A_1 denotes constant integration. Then the electric potential equation is written as [33]:

$$\frac{\mathrm{d}\psi}{\mathrm{d}r} = \frac{1}{\varepsilon_{rr}}\left(e_{rr}\frac{\mathrm{d}u}{\mathrm{d}r} + e_{r\theta}\frac{u}{r} + p_{11}T(r) - \frac{A_1}{r}\right). \tag{12}$$

By substituting, we acquire a differential equilibrium equation in radial displacement u:

$$\begin{aligned} &\frac{\mathrm{d}^2u}{\mathrm{d}r^2} + \left(\frac{\frac{\mathrm{d}m_{11}}{\mathrm{d}r} + H^2\frac{\mathrm{d}\mu}{\mathrm{d}r}}{m_{11}+\mu H^2} + \frac{1}{r}\right)\frac{\mathrm{d}u}{\mathrm{d}r} + \left(\frac{\frac{\mathrm{d}m_{12}}{\mathrm{d}r} + H^2\frac{\mathrm{d}\mu}{\mathrm{d}r}}{r(m_{11}+\mu H^2)} - \frac{m_{22}+\mu H^2}{r^2(m_{11}+\mu H^2)}\right)u + \frac{m_{31}}{m_{11}+\mu H^2}\frac{\mathrm{d}T}{\mathrm{d}r} + \left(\frac{\frac{\mathrm{d}m_{31}}{\mathrm{d}r}}{m_{11}+\mu H^2} + \frac{m_{31}-m_{32}}{r(m_{11}+\mu H^2)}\right)T \\ &- \left(\frac{\frac{\mathrm{d}m_{41}}{\mathrm{d}r}}{r(m_{11}+\mu H^2)} - \frac{m_{42}}{r^2(m_{11}+\mu H^2)}\right)A_1 + \frac{\rho\omega^2 r}{m_{11}+\mu H^2} = 0, \end{aligned} \tag{13}$$

where m_{ij} are functions of r as follows:

$$\begin{aligned} &m_{11} = c_{rr} + \frac{e_{rr}^2}{\varepsilon_{rr}}, \quad m_{12} = c_{r\theta} + \frac{e_{rr}e_{r\theta}}{\varepsilon_{rr}}, \quad m_{22} = c_{\theta\theta} + \frac{e_{r\theta}^2}{\varepsilon_{rr}}, \\ &m_{31} = \frac{e_{rr}p_{11}}{\varepsilon_{rr}} - \lambda_r, \quad m_{32} = \frac{e_{r\theta}p_{11}}{\varepsilon_{rr}} - \lambda_\theta, \quad m_{41} = \frac{e_{rr}}{\varepsilon_{rr}}, \quad m_{42} = \frac{e_{r\theta}}{\varepsilon_{rr}}. \end{aligned} \tag{14}$$

By applying the mathematical algorithm, we obtain a differential equation in temperature, $T(r)$, Eq. (2), as well as a differential Eq. (13) in the radial displacement, $u(r)$, and both equations are functions of the radius, r. Therefore, the resulting differential equations are difficult to solve analytically. In this status, we utilize a semi-analytical method. In the semi-analytical method [40], we separate the radial range into a set of layers, every layer has a thickness $s^{(k)}$ and mean radii of every layer $r^{(k)}$, as appeared in Fig. 2. By writing Eqs. (3) and (13) and calculating the coefficients of the equations at $r = r^{(k)}$, we get:

$$\frac{\mathrm{d}^2T(r^{(k)})}{\mathrm{d}r^2} + G_1^{(k)}\frac{\mathrm{d}T(r^{(k)})}{\mathrm{d}r} = 0, \tag{15}$$

$$\frac{\mathrm{d}^2u^{(k)}}{\mathrm{d}r^2} + N_1^{(k)}\frac{\mathrm{d}u^{(k)}}{\mathrm{d}r} + N_2^{(k)}u^{(k)} + N_3^{(k)} = 0, \tag{16}$$

where,

$$\begin{aligned} &G_1^{(k)} = \left(\frac{1}{r} + \frac{1}{k_T(r)}\frac{\mathrm{d}k_T(r)}{\mathrm{d}r}\right)\Big|_{r=r^{(k)}}, \qquad N_1^{(k)} = \frac{\frac{\mathrm{d}m_{11}}{\mathrm{d}r} + H^2\frac{\mathrm{d}\mu}{\mathrm{d}r}}{(m_{11}+\mu H^2)}\Big|_{r=r^{(k)}} + \frac{1}{r^{(k)}}, \\ &N_2^{(k)} = \frac{\frac{\mathrm{d}m_{12}}{\mathrm{d}r} + H^2\frac{\mathrm{d}\mu}{\mathrm{d}r}}{r(m_{11}+\mu H^2)}\Big|_{r=r^{(k)}} - \frac{m_{22}+\mu H^2}{r^2(m_{11}+\mu H^2)}\Big|_{r=r^{(k)}}, \\ &N_3^{(k)} = \frac{m_{31}}{m_{11}+\mu H^2}\Big|_{r=r^{(k)}}\frac{\mathrm{d}T}{\mathrm{d}r}\Big|_{r=r^{(k)}} + \left(\frac{\frac{\mathrm{d}m_{31}}{\mathrm{d}r}}{(m_{11}+\mu H^2)}\Big|_{r=r^{(k)}} + \frac{m_{31}-m_{32}}{r(m_{11}+\mu H^2)}\Big|_{r=r^{(k)}}\right)T(r^{(k)}) \\ &- \left(\frac{\frac{\mathrm{d}m_{41}}{\mathrm{d}r}}{r(m_{11}+\mu H^2)}\Big|_{r=r^{(k)}} - \frac{m_{42}}{r^2(m_{11}+\mu H^2)}\Big|_{r=r^{(k)}}\right)A_1^{(k)} + \frac{\rho\omega^2 r}{(m_{11}+\mu H^2)}\Big|_{r=r^{(k)}}, \end{aligned} \tag{17}$$

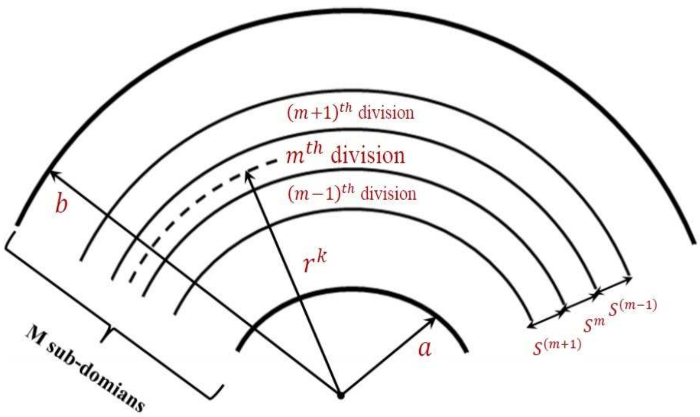

Fig. 2. Divided radii domain to *m* layers by semi-analytical technique.

in which m_{ij} are functions of $r^{(k)}$. By solving differential Eqs. (15) and (16) after using the semi-analytical method, the differential equations are transformed with constant coefficients and the solution is in the formula:

$$T^{(k)} = C_1^{(k)} + C_2^{(k)} e^{-G_1^{(k)} r}, \tag{18}$$

$$u^{(k)} = B_1^{(k)} e^{\delta_1 r} + B_2^{(k)} e^{\delta_2 r} - \frac{N_3^{(k)}}{N_2^{(k)}}, \tag{19}$$

where δ_1, δ_2 reference algebraic roots of $\delta^2 + N_1^{(k)}\delta + N_2^{(k)} = 0$, and $C_1^{(k)}$, $C_2^{(k)}$, $B_1^{(k)}$ and $B_2^{(k)}$ are constants of differential equations for k^{th} layer. The temperature equation (18) and the radial displacement (19) are carried out at:

$$r^{(k)} - \frac{s^{(k)}}{2} \le r \le r^{(k)} + \frac{s^{(k)}}{2}, \tag{20}$$

which $s^{(k)}$ and $r^{(k)}$ are the average radius and radial thickness of k$^{\text{th}}$ layer.

To complete the boundary conditions for each layer, the contact equations must be met for the temperature, stresses, radial displacement, and electrical potential for each two adjacent layers, as follows:

$$\begin{aligned}
&T^{(k)}\Big|_{r=r^{(k)}+\frac{S^{(k)}}{2}} = T^{(k+1)}\Big|_{r=r^{(k+1)}-\frac{S^{(k+1)}}{2}}, \qquad \frac{dT^{(k)}}{dr}\Big|_{r=r^{(k)}+\frac{S^{(k)}}{2}} = \frac{dT^{(k+1)}}{dr}\Big|_{r=r^{(k+1)}-\frac{S^{(k+1)}}{2}},\\
&u^{(k)}\Big|_{r=r^{(k)}+\frac{S^{(k)}}{2}} = u^{(k+1)}\Big|_{r=r^{(k+1)}-\frac{S^{(k+1)}}{2}}, \qquad \sigma_r^{(k)}\Big|_{r=r^{(k)}+\frac{S^{(k)}}{2}} = \sigma_r^{(k+1)}\Big|_{r=r^{(k+1)}-\frac{S^{(k+1)}}{2}},\\
&\psi^{(k)}\Big|_{r=r^{(k)}+\frac{S^{(k)}}{2}} = \psi^{(k+1)}\Big|_{r=r^{(k+1)}-\frac{S^{(k+1)}}{2}}, \qquad \frac{d\psi^{(k)}}{dr}\Big|_{r=r^{(k)}+\frac{S^{(k)}}{2}} = \frac{d\psi^{(k+1)}}{dr}\Big|_{r=r^{(k+1)}-\frac{S^{(k+1)}}{2}}.
\end{aligned} \tag{21}$$

Combining boundary conditions for case 1, Eq. (9), or case 2 of the boundary conditions, Eq. (10), with the continuity equations (21), a system of algebraic equations is generated regarding constants $A_1^{(k)}$, $A_2^{(k)}$, $B_1^{(k)}$, $B_2^{(k)}$, $C_1^{(k)}$, $C_2^{(k)}$, $(k = 1,2,\dots,m)$. By resolving them together, we can obtain the value of the temperature and the radial displacement, and from them, we can calculate the worth of the stresses and electric potential for each layer k^{th} $(k = 1,2,\dots,m)$.

Table 2. Comparison among various porosity distributions on FG piezoelectric hollow cylinder in mechanical pressure and electrical loading.

Variable	$\bar{r}$	Perfect FGPM ($\beta=0$)			Even FGPM ($\beta=0.1$)			Uneven I FGPM ($\beta=0.1$)			Uneven II FGPM ($\beta=0.1$)		
		$n=5$	$n=10$	$n=20$	$n=5$	$n=10$	$n=20$	$n=5$	$n=10$	$n=20$	$n=5$	$n=10$	$n=20$
$\bar{T}$	0.3	1.0494	1.0562	1.0605	1.0217	1.0568	1.0127	1.0086	1.0237	1.0449	1.0537	1.0608	1.0651
	0.5	1.1091	1.1241	1.1335	1.0479	1.1253	1.0279	1.0195	1.0534	1.1011	1.1161	1.1312	1.1404
	0.7	1.1501	1.1689	1.1818	1.0662	1.1707	1.0381	1.0274	1.0742	1.1402	1.1566	1.1754	1.1877
$\bar{u}\times 10^2$	0.3	2.9806	2.6873	2.6516	5.2401	5.2327	3.1449	3.9206	3.4826	3.4779	3.3948	2.9829	2.9966
	0.5	1.6943	1.3908	1.3676	3.5241	3.5498	1.1618	2.6271	2.1228	2.1235	1.8936	1.4809	1.5119
	0.7	0.9682	0.6397	0.6246	2.7218	2.7816	-0.0841	2.0443	1.4121	1.4189	1.0659	0.6407	0.6869
$\bar{\sigma}_r$	0.3	-0.2065	-0.2591	-0.2631	-0.1438	-0.1417	-0.3969	-0.1062	-0.1856	-0.1859	-0.2494	-0.3035	-0.2999
	0.5	0.0434	-0.0281	-0.0321	0.1594	0.1676	-0.2051	0.1949	0.0771	0.0768	0.0129	-0.0581	-0.0516
	0.7	-0.0028	-0.0596	-0.0604	0.1591	0.1835	-0.2148	0.1939	0.0693	0.0709	-0.0152	-0.0674	-0.0575
$\bar{\sigma}_\theta$	0.3	0.6972	0.5693	0.5619	0.9912	0.9495	0.3101	0.9823	0.8108	0.8103	0.6009	0.4662	0.4791
	0.5	0.1171	0.0254	0.0234	0.3487	0.3619	-0.1333	0.3469	0.2019	0.2021	0.1072	0.0099	0.0229
	0.7	-0.0709	-0.1428	-0.1423	0.1637	0.1859	-0.2602	0.1635	0.0381	0.0393	-0.0703	-0.1465	-0.1331
$\bar{\psi}$	0.3	0.6112	0.6253	0.6216	0.4251	0.4168	0.5781	0.5241	0.5579	0.5571	0.5629	0.5819	0.5745
	0.5	0.3624	0.3716	0.3606	0.1439	0.1259	0.3255	0.2384	0.2786	0.2767	0.3128	0.3249	0.3093
	0.7	0.2412	0.2394	0.2228	0.0887	0.0708	0.2059	0.1348	0.1592	0.1574	0.2112	0.2093	0.1892

Table 3. Comparison among various porosity distributions on FG piezoelectric mounted hollow cylinder and electrical loading.

Variable	$\bar{r}$	Perfect FGPM ($\beta=0$)			Even FGPM ($\beta=0.1$)			Uneven I FGPM ($\beta=0.1$)			Uneven II FGPM ($\beta=0.1$)		
		$n=5$	$n=10$	$n=20$	$n=5$	$n=10$	$n=20$	$n=5$	$n=10$	$n=20$	$n=5$	$n=10$	$n=20$
$\bar{T}$	0.3	1.0494	1.0562	1.0605	1.0217	1.0568	1.0127	1.0086	1.0237	1.0449	1.0537	1.0607	1.0651
	0.5	1.1091	1.1241	1.1335	1.0479	1.1253	1.0279	1.0195	1.0534	1.1011	1.1161	1.1312	1.1404
	0.7	1.1501	1.1689	1.1818	1.0662	1.1707	1.0381	1.0274	1.0742	1.1402	1.1566	1.1754	1.1877
$\bar{u}\times 10^2$	0.3	-0.6401	-0.6641	-0.6477	-0.3747	-0.2966	-0.8153	-0.2963	-0.3618	-0.3461	-0.9858	-1.0181	-0.9768
	0.5	-1.7131	-1.7678	-1.7239	-1.0643	-0.8582	-2.1586	-0.8269	-1.0009	-0.9543	-2.4631	-2.5282	-2.4301
	0.7	-2.7451	-2.8019	-2.7308	-1.7464	-1.4138	-3.4006	-1.3617	-1.6481	-1.5667	-3.7087	-3.7599	-3.6164
$\bar{\sigma}_r$	0.3	0.2509	0.1991	0.2006	0.4415	0.5565	0.1088	0.6288	0.5315	0.5276	-0.0532	-0.1031	-0.0835
	0.5	-0.2051	-0.2414	-0.2306	0.1153	0.1528	-0.2045	0.2119	0.1227	0.1308	-0.3713	-0.4027	-0.3781
	0.7	-0.4826	-0.4831	-0.4641	-0.0639	-0.0015	-0.3645	-0.0089	-0.0892	-0.0732	-0.5766	-0.5661	-0.5351
$\bar{\sigma}_\theta$	0.3	-0.9631	-0.9801	-0.9558	-0.4371	-0.3697	-0.7228	-0.5245	-0.5813	-0.5584	-1.0113	-1.0281	-0.9888
	0.5	-0.9878	-1.0121	-0.9873	-0.4202	-0.3549	-0.7366	-0.4582	-0.5294	-0.5071	-1.0771	-1.0991	-1.0588
	0.7	-0.9743	-1.0179	-0.9955	-0.3901	-0.3478	-0.7335	-0.3968	-0.4936	-0.4736	-1.0761	-1.1193	-1.0824
$\bar{\psi}$	0.3	0.4921	0.4716	0.4552	0.5091	0.4718	0.4809	0.4903	0.4679	0.4479	0.4771	0.4523	0.4356
	0.5	0.9699	0.9259	0.8912	1.0107	0.9234	0.9388	0.9729	0.9218	0.8801	0.9507	0.8987	0.8628
	0.7	1.1584	1.1051	1.0604	1.2317	1.1119	1.1123	1.1843	1.1117	1.0592	1.1431	1.0824	1.0361

8. Numerical Product and Discussion

By following a series of procedures to study the even distribution and uneven logarithmic distribution of porosity on a hollow cylinder of FGM rotating around a fixed axis with constant angular velocity ω in a stable magnetic field. The logarithmic distribution is presented for two cases of uneven porosity distribution. The cylinder is also subjected to Lorentz force arising from the magnetic domain, electric field, and the inertia force resulting from rotation, as well as a thermal effect, with the thermal and physical properties coefficients gradually increasing towards the radius of the cylinder. A comparison was presented between the status of a non-porous (perfect) cylinder and the status of a porous cylinder with different porosity distributions for temperature, stresses, electric potential, and radial displacement to confirm the precision and competence of the semi-analytical technique. After that, the influence of the homogeneity coefficient n and the porosity coefficient β at different positions of the cylinder was studied. The final part of the study was to explore the influence of variables on two various cases of boundary conditions, the first case of a porous cylinder is traction-free, and the second case of a porous cylinder is fixed from the inside. Numerical results and illustrative graphics are presented for each case separately, with comparison tables for the different distributions presented in Tables 2 and 3. We assume that the following non-dimensional variables are:

$$\bar{r} = \frac{r}{b}, \quad \bar{u} = \frac{u}{b} \times 10^2, \quad \bar{T}(\bar{r}) = \frac{T(\bar{r})}{T_0}, \quad \bar{\psi}(\bar{r}) = \frac{\psi(\bar{r})}{\psi_2}, \quad \bar{\sigma}_i(\bar{r}) = \frac{\sigma_i(\bar{r})}{P_2}, \quad i = r, \theta. \tag{22}$$

- Case 1 (Free-Free) Mechanical pressure and electrical loading on hollow porous cylinder

$$\sigma_r|_{r=a} = -10^{10} Pa, \quad \sigma_r|_{r=b} = 0, \quad \psi(r)|_{r=a} = 10^8 W/A, \quad \psi(r)|_{r=b} = 0.$$

The first status of boundary conditions is the state of a free-moving cylinder, where the internal surface of the cylinder is exposed to constant pressure while the external surface of the cylinder is free to move. Also, the external surface of the cylinder is grounded. First, a numeric comparison is presented for various amounts of grading index n at various positions of the cylinder for temperature, stresses, electrical potential, and radial displacement for different distributions of porosity. It is noted from Table 2 that:

- Temperature $\bar{T}$ achieves its highest value at various amounts of the grading index n in uneven II logarithmic distribution with multiple positions.
- The radial displacement $\bar{u}$ achieves the highest value in the case of $n = 5, 10$ at the value of even distribution, while at the value of $n = 20$ it achieves the highest value in uneven I logarithmic distribution.
- Radial stress $\bar{\sigma}_r$ achieves the highest value in uneven I logarithmic distribution in the case of $n = 5, 20$ while when $n = 10$ it is achieved in even distribution.
- Hoop stress $\bar{\sigma}_\theta$, the results agree with the radial displacement $\bar{u}$, as the highest value is done at $n = 5, 10$ in even distribution, and the highest value is $n = 20$ in uneven I logarithmic distribution.
- The electrical potential $\bar{\psi}$ achieved the highest value in the case of a non-porous (perfect) cylinder depending on the value of grading index n and position.

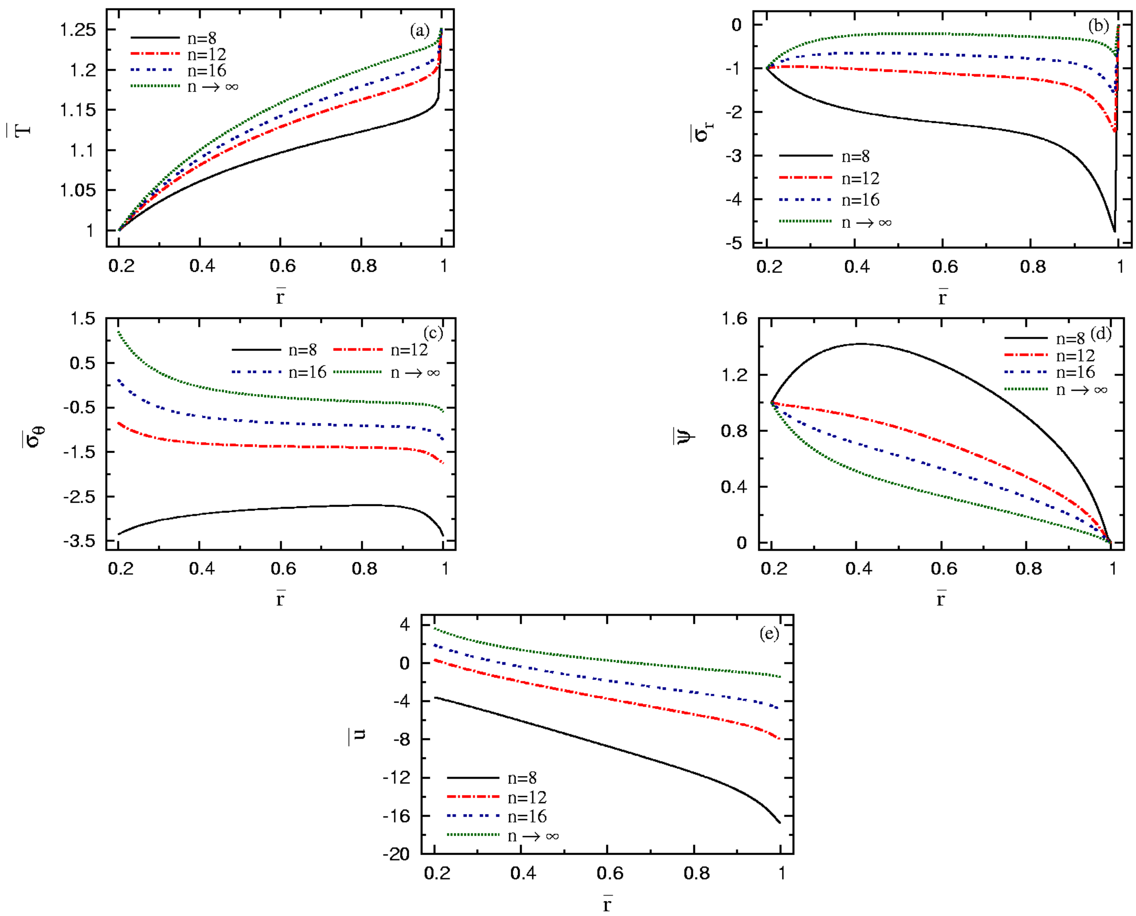

Fig. 3. Influence of grading index in even porosity distribution on mechanical pressure and electrical loading on FG cylinder.

Figure 3 illustrates the effect of the gradient coefficient n on the porous cylinder under the influence of mechanical pressure and electric field at different values of the gradient coefficient $n = 8$, 12, 16, and $n \longrightarrow \infty$ in the status of an even distribution of porosity. Figure 3a shows the effect of the gradient factor n on the temperature distribution $\bar{T}$ on the porous cylinder, and from the results, it is evident that the temperature value $\bar{T}$ increases by an increase in gradient factor n, where the highest temperature value $\bar{T}$ is achieved at $n \longrightarrow \infty$ and the lowest value is achieved at $n = 8$. While Fig. 3b shows the value of radial stress $\bar{\sigma}_r$ at various values of gradient factor n, and its result agrees with the temperature value $\bar{T}$, as the value of radial stress $\bar{\sigma}_r$ increases by an increase of n, fulfilling boundary conditions for the radial stress $\bar{\sigma}_r$, where it equals one at the internal surface $\bar{r} = a/b$ of the cylinder and disappears at the external surface $\bar{r} = 1$ of cylinder. Figure 3c also presented a value of hoop stress $\bar{\sigma}_\theta$ with change in gradient factor n, where the value of hoop stress $\bar{\sigma}_\theta$ increases by an increase in gradient factor n. Value of electric potential $\bar{\psi}$ is displayed in Fig. 3d, which fulfilled boundary conditions, where electric potential $\bar{\psi}$ equals one at internal radii $\bar{r}$ of the cylinder, then the value of the electric potential $\bar{\psi}$ starts to lower in the orientation of radii, achieving zero on the outer surface $\bar{r} = 1$ of the cylinder. As for the radial displacement $\bar{u}$, it is appeared in Fig. 3e, where value of radial displacement $\bar{u}$ curves decrease in the direction of the radius of the cylinder from the inside to the outside. At $n \longrightarrow \infty$, the highest amount of radial displacement $\bar{u}$ appears, while at $n = 8$, lowest value of radial displacement $\bar{u}$ occurs.

A study of the effectiveness of the porosity coefficient on the FG cylinder in the status of an even porosity distribution was studied in Fig. 4 for the porosity coefficients $\beta = 0.3, 0.5, 0.7, 0.9$, and the case of non-porosity $\beta = 0$. Figure 4a shows the temperature $\bar{T}$ at various values of the porosity coefficient β, and it is clear that the highest temperature $\bar{T}$ value is achieved in the case of $\beta = 0.5$ and the lowest value of temperature $\bar{T}$ is achieved at $\beta = 0.3$. From the Fig. 4a, it also appears that temperature curves $\bar{T}$ increase in the direction of the radius, fulfilling temperature boundary conditions. The radial stress $\bar{\sigma}_r$ is presented in Fig. 4b, from which it seems that curves are increasing in the direction of the radius, fulfilling boundary conditions for stress. It is also evident that the highest amount of radial stress $\bar{\sigma}_r$ is at $\beta = 0.5$ and the lowest value is at $\beta = 0.9$. As for the hoop stress $\bar{\sigma}_\theta$, it was shown in Fig. 4c, where the curves decrease from $\bar{r} = 0.2$ to $\bar{r} = 1$, also achieving the highest value at $\beta = 0.5$ and the lowest value at $\beta = 0.3$. Figure 4d shows the value of electric potential $\bar{\psi}$ on cylinder for different values of porosity coefficient β, where curves begin to decrease from $\bar{r} = 0.2$ until $\bar{r} \cong 0.45$ and then begin to increase again until $\bar{r} = 1$, fulfilling boundary conditions for electric potential $\bar{\psi}$. It also appears from the figure that the highest value of electric potential $\bar{\psi}$ is in status of non-porous cylinder $\beta = 0$, then value of electric potential $\bar{\psi}$ begins to decrease with the increase in porosity factor β, achieving the lowest value of electric potential $\bar{\psi}$ at $\beta = 0.9$. Radial displacement $\bar{u}$ is illustrated in Fig. 4e, where curves begin to decrease from $\bar{r} = 0.2$ until $\bar{r} = 1$. The highest value of radial displacement $\bar{u}$ is achieved at the highest value of porosity coefficient β, and lowest value of radial displacement $\bar{u}$ is achieved in the status of $\beta = 0$, that is, in the case of a perfect cylinder.

In the status of uneven I logarithmic distribution, the influence of the gradient coefficient n on the cylinder was offered and studied for various values of $n = 8,12,16$ and $n \longrightarrow \infty$. Figure 5a displayed the effectiveness of the gradient factor n on temperature $\bar{T}$ in the case of uneven I logarithmic distribution, and its results agreed with Fig. 3a in the case of an even distribution. The behavior of the radial stress curves $\bar{\sigma}_r$ in the case of the uneven I logarithmic distribution of porosity also agreed with the even distribution at several values of gradient factor in Fig. 5b.

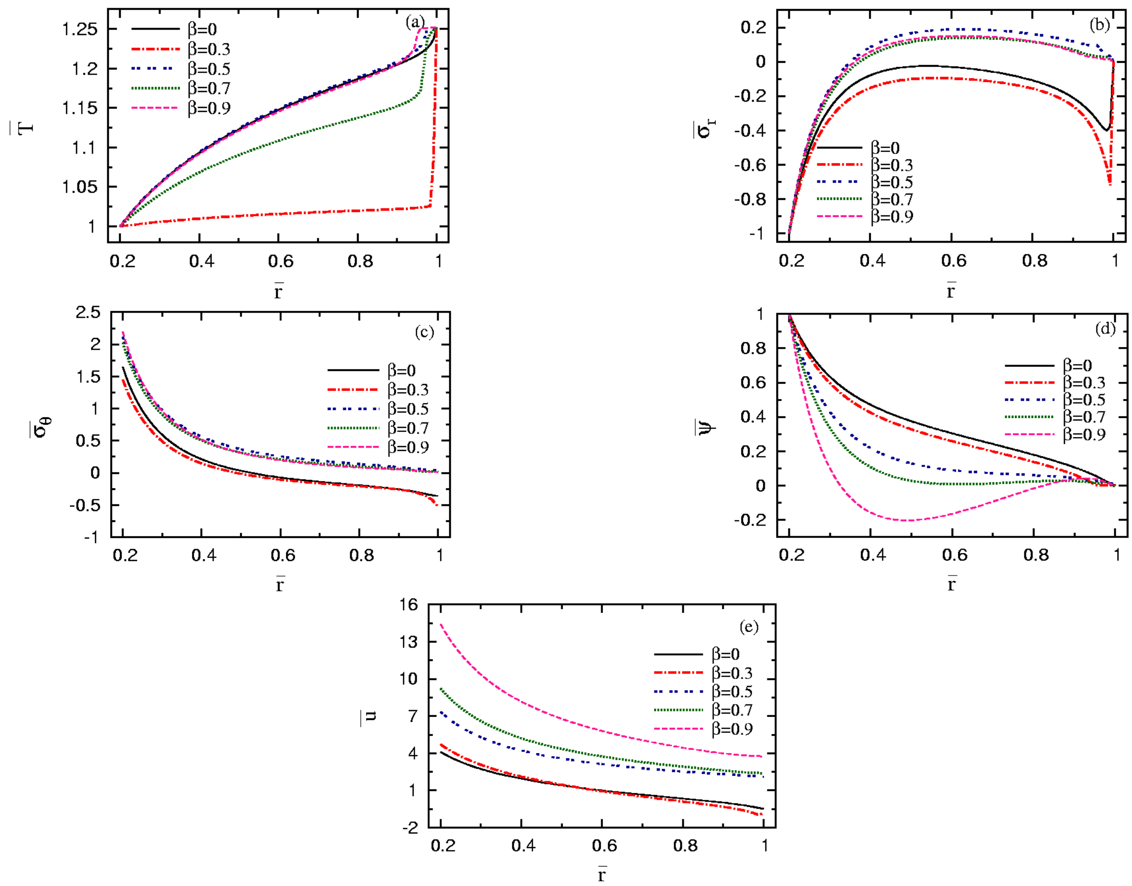

Fig. 4. Effectiveness of porosity parameter in even porosity distribution on mechanical pressure and electrical loading on FG cylinder.

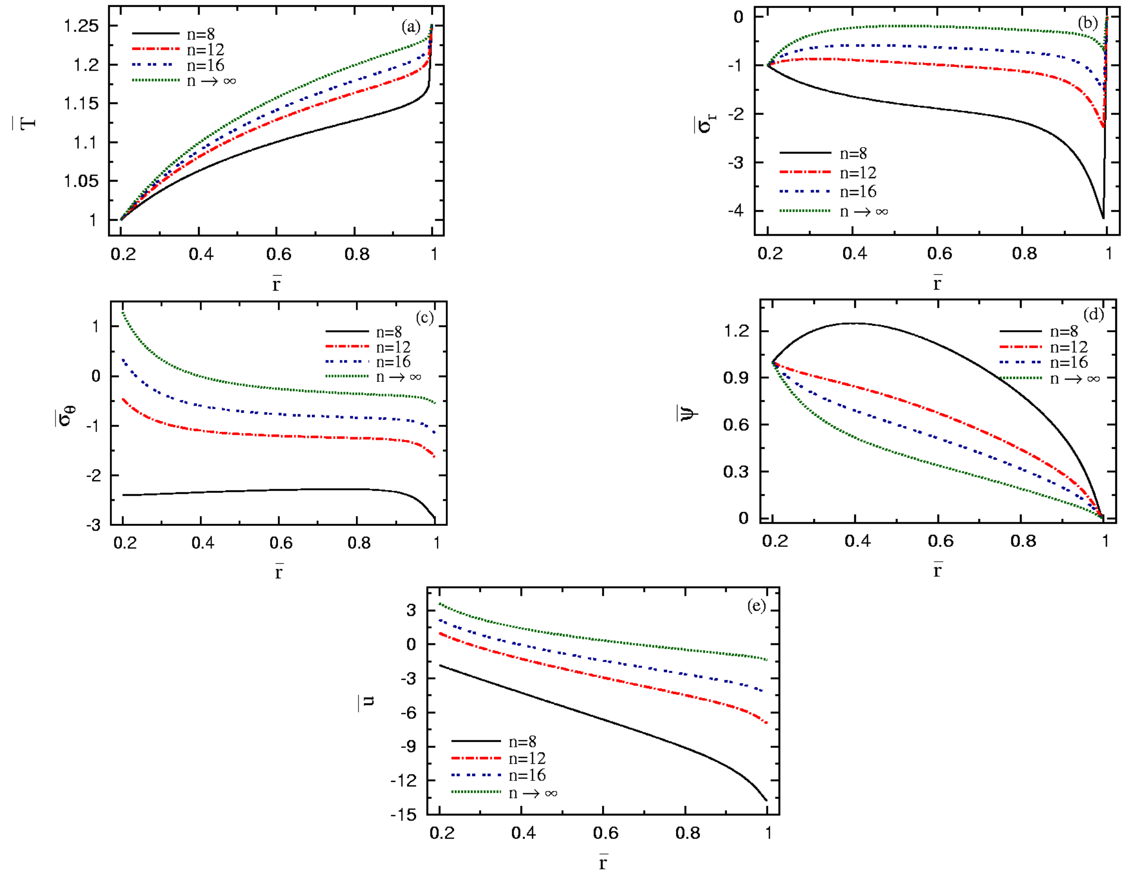

Fig. 5. Influence of grading index in uneven I porosity distribution on mechanical pressure and electrical loading on FG cylinder.

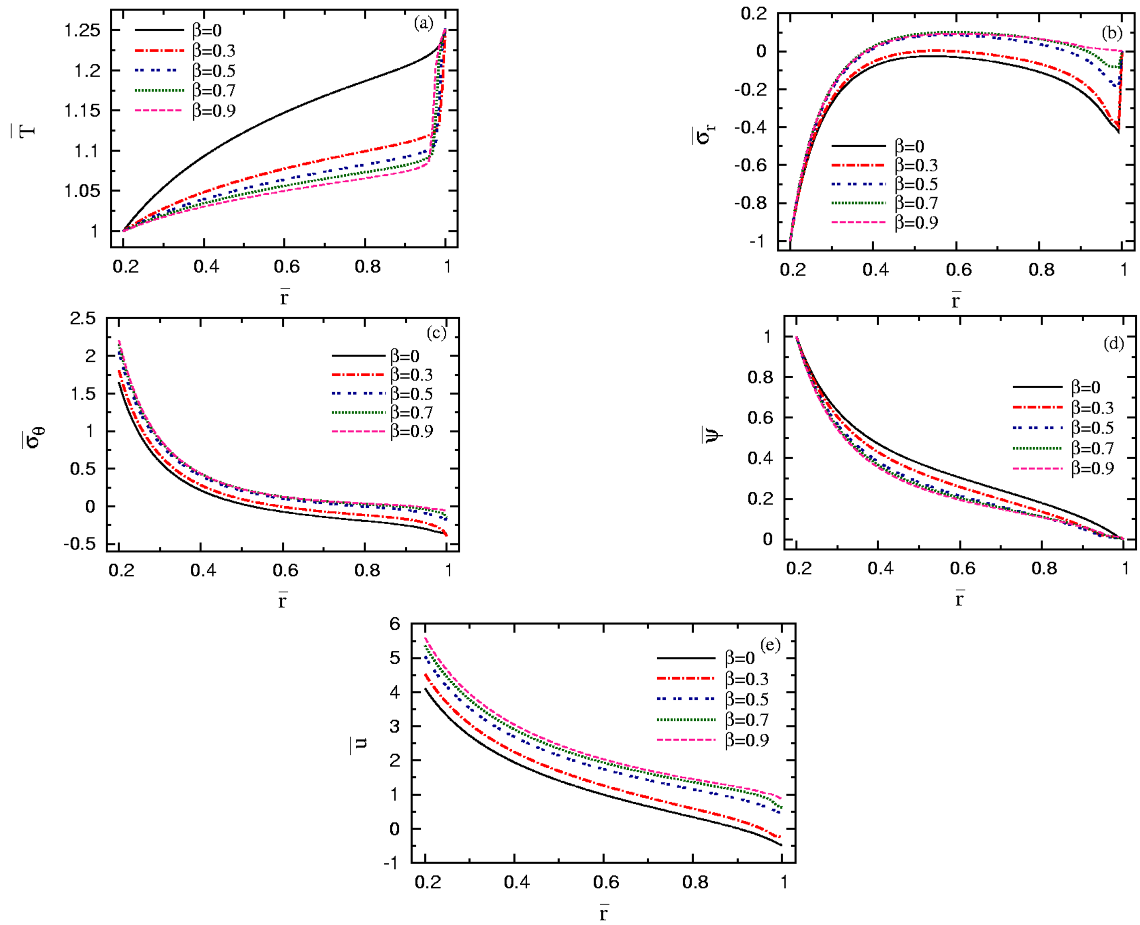

Fig. 6. Effectiveness of porosity parameter in uneven I porosity distribution on mechanical pressure and electrical loading on FG cylinder.

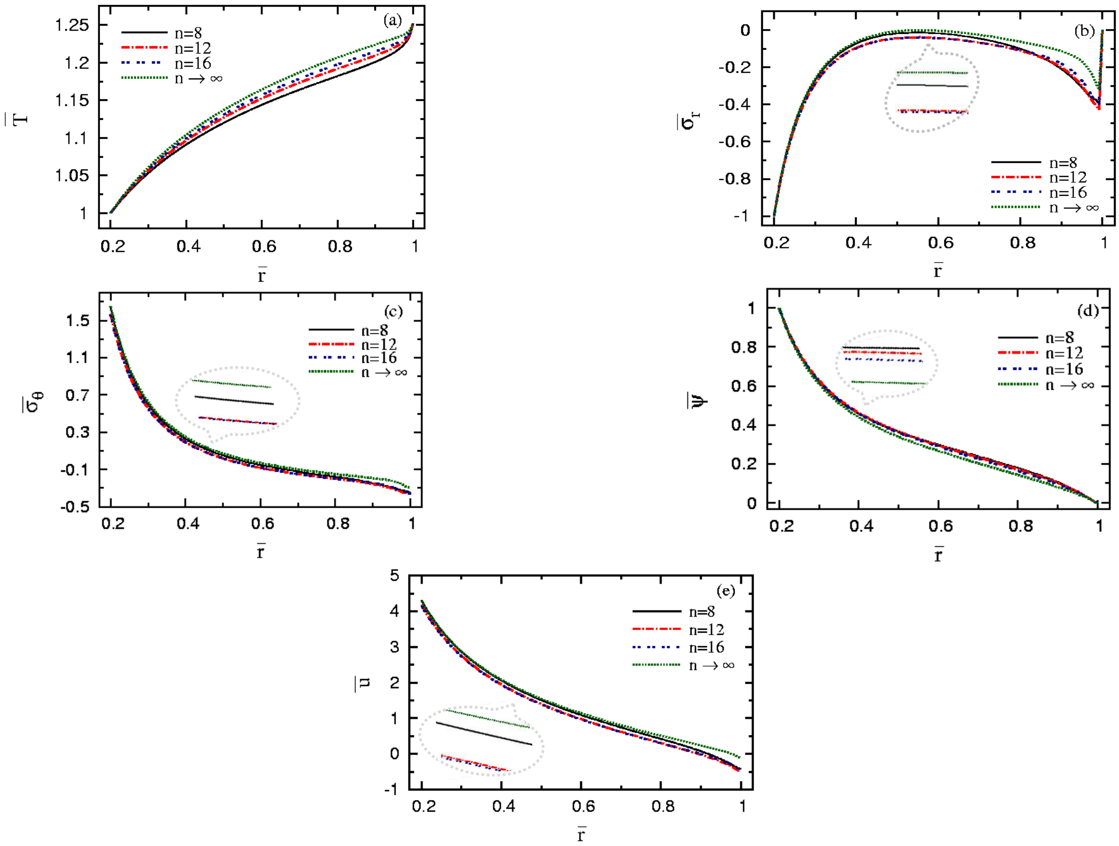

Fig. 7. Influence of grading index in uneven II porosity distribution on mechanical pressure and electrical loading on FG cylinder.

Hoop stress $\bar{\sigma}_\theta$ is appeared in Fig. 5c and it appears that with an increase in the gradient factor n, the value of hoop stress $\bar{\sigma}_\theta$ grows, as the highest value of hoop stress $\bar{\sigma}_\theta$ is achieved at $n \longrightarrow \infty$ and the lowest value is achieved in the case of $n = 8$. The electric potential $\bar{\psi}$ Is studied in Fig. 5d, and it appears that the curves fulfill the boundary conditions for electric potential $\bar{\psi}$ at the edges. Also, by increasing the gradient factor n, the value of the electric potential $\bar{\psi}$ decreases, achieving the highest value for the electric potential $\bar{\psi}$ at $n = 8$ and the lowest value at $n \longrightarrow \infty$. Figure 5e demonstrates the value of radial displacement $\bar{u}$ at various values of gradient factor n, where radial displacement $\bar{u}$ grows with the increase in gradient factor n, achieving the lowest value of radial stress when $n = 8$ and the highest value at $n \longrightarrow \infty$.

The second part of the study of uneven I logarithmic distribution is to study the effectiveness of porosity coefficient β on temperature and stresses at several values of porosity coefficient $\beta = 0,0.3,0.5,0.7$ and $\beta = 0.9$ in Fig. 6. The temperature curves $\bar{T}$ with variation in the porosity parameter β appear in Fig. 6a, and it clarifies that the highest value of temperature $\bar{T}$ is appeared in the status of the non-porous cylinder $\beta = 0$, and the lowest value of temperature $\bar{T}$ is appeared in the status of the highest value of the porosity coefficient, $\beta = 0.9$. Effectiveness of porosity parameter β on radial stress $\bar{\sigma}_r$ differs from its effect on temperature $\bar{T}$, as it appears from Fig. 6b that the lowest value of radial stress $\bar{\sigma}_r$ is appeared in the status of a non-porous cylinder $\beta = 0$, and the highest value of radial stress $\bar{\sigma}_r$ is appeared in the status of the highest value of porosity factor $\beta = 0.9$. In Fig. 6c, the behavior of hoop stress $\bar{\sigma}_\theta$ is achieved with the behavior of the radial stress $\bar{\sigma}_\theta$, where the value of hoop stress $\bar{\sigma}_\theta$ grows with a rise in porosity factor β, achieving the highest value of hoop stress $\bar{\sigma}_\theta$ at $\beta = 0.9$. Electric potential $\bar{\psi}$ curves were studied in Fig. 6d, where value of electric potential $\bar{\psi}$ reduces towards radius and value of electric potential $\bar{\psi}$ reduces with the increase in porosity factor β, where the electric potential $\bar{\psi}$ achieves the highest value in status of the non-porous cylinder $\beta = 0$ and the lowest value of electric potential $\bar{\psi}$ is at $\beta = 0.9$. The radial displacement $\bar{u}$ was reviewed in Fig. 6e, several values of porosity factor β along the radius of the cylinder, where radial displacement $\bar{u}$ decreases in the orientation of the radius from the inside to the outside. Radial displacement $\bar{u}$ is affected by porosity factor β, as the radial displacement $\bar{u}$ grows with an increase in porosity factor β, achieving the lowest value of radial displacement $\bar{u}$ in the status of perfect cylinder $\beta = 0$ and the highest value of radial displacement when $\beta = 0.9$.

To survey uneven II logarithmic distribution on the porous cylinder, study the effect of the gradation coefficient $n = 8,12,16$ and $n \longrightarrow \infty$ in Fig. 7, and study the effect of the porosity coefficient $\beta = 0,0.3,0.5,0.7$ and $\beta = 0.9$ in Fig. 8. In Fig. 7a, the temperature $\bar{T}$ is appeared with a change in the gradient factor n, and it is evident from it that the temperature value $\bar{T}$ increases with rise in the gradient factor n, as the greatest value of temperature $\bar{T}$ is appeared at $n \longrightarrow \infty$ and the lowest value of temperature $\bar{T}$ is appeared at $n = 8$. Radial stress $\bar{\sigma}_r$ and effectiveness of gradient factor n on it is presented in Fig. 7b. It appears from its graph that the highest value of radial stress $\bar{\sigma}_r$ is achieved at $n \longrightarrow \infty$ and lowest value of radial stress $\bar{\sigma}_r$ is appeared at $n = 16$. It is also evident from its graph that radial stress increases in the direction of the radius from the inside to the outside, fulfilling boundary conditions for stresses on porous cylinder. Figure 7c illustrates the hoop stress $\bar{\sigma}_\theta$ with a change in the gradient factor n. It appears from the graph that the hoop stress curves $\bar{\sigma}_\theta$ are almost identical with a change in the gradient factor n and the highest value of hoop stress $\bar{\sigma}_\theta$ is achieved at $n \longrightarrow \infty$. Electric potential $\bar{\psi}$ in the case of an uneven II logarithmic distribution is presented in Fig. 7d. From the graph it appears that the value of electric potential $\bar{\psi}$ reduces with an increase in gradient factor n. Thus, electric potential $\bar{\psi}$ achieves the highest value in status of the non-porous cylinder and the lowest value of electric potential $\bar{\psi}$ at $n \longrightarrow \infty$. As for the radial displacement $\bar{u}$, it was displayed in Fig. 7e with the variation in gradient factor n, achieving the highest value for radial displacement at $n \longrightarrow \infty$. It is also evident from the graph that radial displacement curves reduce the orientation of the radius of the cylinder from the inside to the outside.

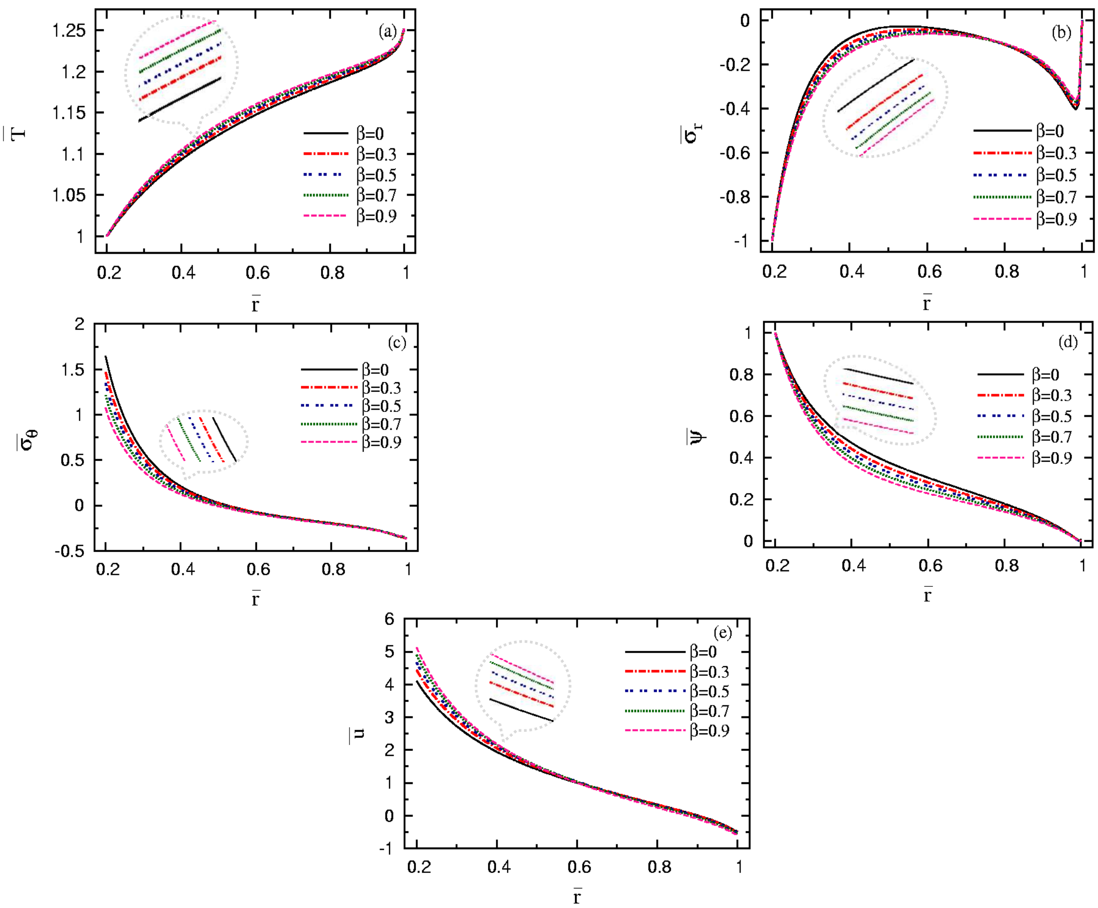

Fig. 8. Effectiveness of porosity parameter in uneven II porosity distribution on mechanical pressure and electrical loading on FG cylinder.

A study of the effectiveness of porosity factor β on the cylinder in the status of uneven II logarithmic distribution appears in Fig. 8. The survey of the influence of porosity coefficient β on temperature $\bar{T}$ was presented in Fig. 8a, where the temperature curves $\bar{T}$ correspond to the change in the porosity coefficient β. It appears from its graph that the greater value of porosity coefficient β, the greater the temperature $\bar{T}$ value, and thus the lowest temperature $\bar{T}$ value is achieved in the non-porous cylinder $\beta = 0$. Figure 8b illustrates radial stress with a change in porosity coefficient β, where the value of the radial stress reduces with an increase in porosity coefficient β, achieving lowest value of radial stress in status of the non-porous cylinder. As for the hoop stress, it was illustrated in Fig. 8c. It appears from graph that the hoop stress value decreases in orientation of radius. Also, the hoop stress reduces with raise in porosity factor β, as the highest value of hoop stress is appeared in status of perfect cylinder. Electric potential $\bar{\psi}$ is offered and studied with the variation in porosity factor β, and it appears that the value of electric potential reduces with an increase in porosity coefficient and that lowest value of electric potential $\bar{\psi}$ is achieved in the case of the highest value of the porosity coefficient β with $\beta = 0.9$. Figure 8e displays value of radial displacement $\bar{u}$ with the variation in porosity factor β. Value of radial displacement $\bar{u}$ decreases as value of porosity factor β decreases. Therefore, lowest value of radial displacement $\bar{u}$ is appeared in status of a non-porous cylinder.

- Case 2 (Fixed-Free) mounted hollow porous cylinder

$$u(r)|_{r=a} = 0, \quad \sigma_r|_{r=b} = -10^{10} Pa, \quad \psi(r)|_{r=a} = 0, \quad \psi(r)|_{r=b} = 10^8 \ W/A.$$

The second case survey porous cylinder made of a material with gradient properties, fixed from the inside and subjected to constant pressure from the outside. The purpose of mounting from the inside is to protect fragile, porous materials and to obtain optimal edge protection to protect the layers. It also allows for more efficient and safe handling of the non-porous cylinder. The cylinder is also exposed to an external electric field while the inner surface remains grounded. To show the comparison between the even distribution of porosity and uneven logarithmic porosity distribution in I and II, as well as in the status of a non-porous (perfect) cylinder at different values of the gradation coefficient n and at different positions $\bar{r}$ and the porosity coefficient $\beta = 0.1$, from which it becomes clear that:

- The temperature value $\bar{T}$ achieved its highest value in the status of uneven II logarithmic distribution for all values of the gradient coefficient n.
- Radial displacement $\bar{u}$ achieved its highest value in the case of uneven I logarithmic distribution when $n = 5,20$. However, in the case of $n = 10$, the radial displacement had the highest value in the status of the even distribution.
- Radial stress $\bar{\sigma}_r$ values agreed with the radial displacement values $\bar{u}$, as the highest value has appeared in the status of uneven II logarithmic distribution when $n = 5,20$, and highest value of radial stress $\overline{\sigma_r}$ is appeared in the case of an even distribution when $n = 10$.
- The hoop stress $\bar{\sigma}_\theta$ value achieved the highest value in status of an even distribution of porosity in status of $n = 5,10$, while at $n = 20$ it achieved the highest value in status of uneven I logarithmic distribution.
- Electrical potential $\bar{\psi}$ achieved the greatest results in the case of an even distribution at different values of the gradient factor n and at all positions inside the cylinder.

Figure 9 presents the results of applying the even porosity distribution to temperature and stresses at different values of the gradient factor $n = 8{,}12{,}16$ and $n \longrightarrow \infty$. As shown in Fig. 9a, the distribution of temperature $\bar{T}$ at various values of the gradient coefficient n, and from the graph it appears that the temperature value $\bar{T}$ increases with increasing gradient coefficient n. As for Fig. 9b, the radial stress $\bar{\sigma}_r$ curves appear with the change in the gradient factor n, and from it appears that the value of radial stress curves grows with a rise in gradient factor n and the lowest value of radial stress $\bar{\sigma}_r$ in status $n = 8$. The hoop stress $\bar{\sigma}_\theta$ value in Fig. 9c also agrees with the radial stress $\bar{\sigma}_r$ result in Fig. 9b. As for Fig. 9d, it displays curves of electric potential $\bar{\psi}$ with the variation in the gradient coefficient n, as there is an inverse relation among electric potential $\bar{\psi}$ and gradient coefficient n. The greater the value of gradient factor n, the lower value of electric potential $\bar{\psi}$. As for the radial displacement $\bar{u}$, it has appeared in Fig. 9e, and it displays a direct relation among gradient coefficient n and radial displacement $\bar{u}$, achieving the highest value for the radial displacement $\bar{u}$ at $n \longrightarrow \infty$.

The second part of the study of the even porosity distribution and its relationship to the porosity coefficient was presented in Fig. 10 at several values of porosity coefficient $\beta = 0{,}0.3{,}0.5{,}0.7$ and $\beta = 0.9$. Figure 10a shows the temperature curves $\bar{T}$ with a change in the porosity coefficient β. The lowest temperature $\bar{T}$ value is when $\beta = 0.3$. The radial stress $\bar{\sigma}_r$ is shown in Fig. 10b, and it is evident from the graph that the greater the value of porosity factor β, the greater the value of the radial stress $\bar{\sigma}_r$ at most points, and the lowest radial stress $\bar{\sigma}_r$ is appeared in the status of a non-porous cylinder. Hoop stress $\bar{\sigma}_\theta$ is appeared in Fig. 10c and the graph shows that there is a direct relation between porosity parameter β and hoop stress $\bar{\sigma}_\theta$, where the hoop stress $\bar{\sigma}_\theta$ records the lowest value in the case of a perfect cylinder. As for the electrical potential $\bar{\psi}$, it was displayed in Fig. 10d with variation in porosity parameter β, and lowest value of electrical potential $\bar{\psi}$ is recorded at $\beta = 0.9$. The radial displacement $\bar{u}$ was displayed in Fig. 10e, where the lowest value of radial displacement $\bar{u}$ is recorded at $\beta = 0.3$ and the largest value was recorded at $\beta = 0.9$.

Figure 11 displays uneven I logarithmic distribution and the effect of the gradient factor n on temperature $\bar{T}$, stresses $\bar{\sigma}_r$, $\bar{\sigma}_\theta$ and electrical potential $\bar{\psi}$. By comparing Fig. 11 and Fig. 9, it is clear that the temperature $\bar{T}$, radial stress $\bar{\sigma}_r$, hoop stress $\bar{\sigma}_\theta$, electric potential $\bar{\psi}$, and radial displacement $\bar{u}$, respectively, followed the same behavior as Fig. 9 with the change in the gradient coefficient n.

Figure 12 illustrates the influence of porosity parameter β in the status of uneven I logarithmic distribution, and it is clear that Fig. 12a regarding the temperature curves $\bar{T}$ follow an inverse relationship with the value of the porosity coefficient β, since by increasing porosity coefficient β, temperature $\bar{T}$ value increases. As for Fig. 12b for the radial stress $\bar{\sigma}_r$, Figure 12c for the hoop stress $\bar{\sigma}_\theta$ curves, and Fig. 12e for the radial displacement $\bar{u}$, they all have a direct relation with the porosity coefficient β, as the value of the curve grows with a rise in the value of porosity coefficient β. Figure 12d shows a value of electrical potential $\bar{\psi}$ with variation in porosity parameter β. It turns out that the highest value of electrical potential $\bar{\psi}$ is achieved when $\beta = 0.7$, and the lowest value of electrical potential $\bar{\psi}$ is appeared when $\beta = 0.9$.

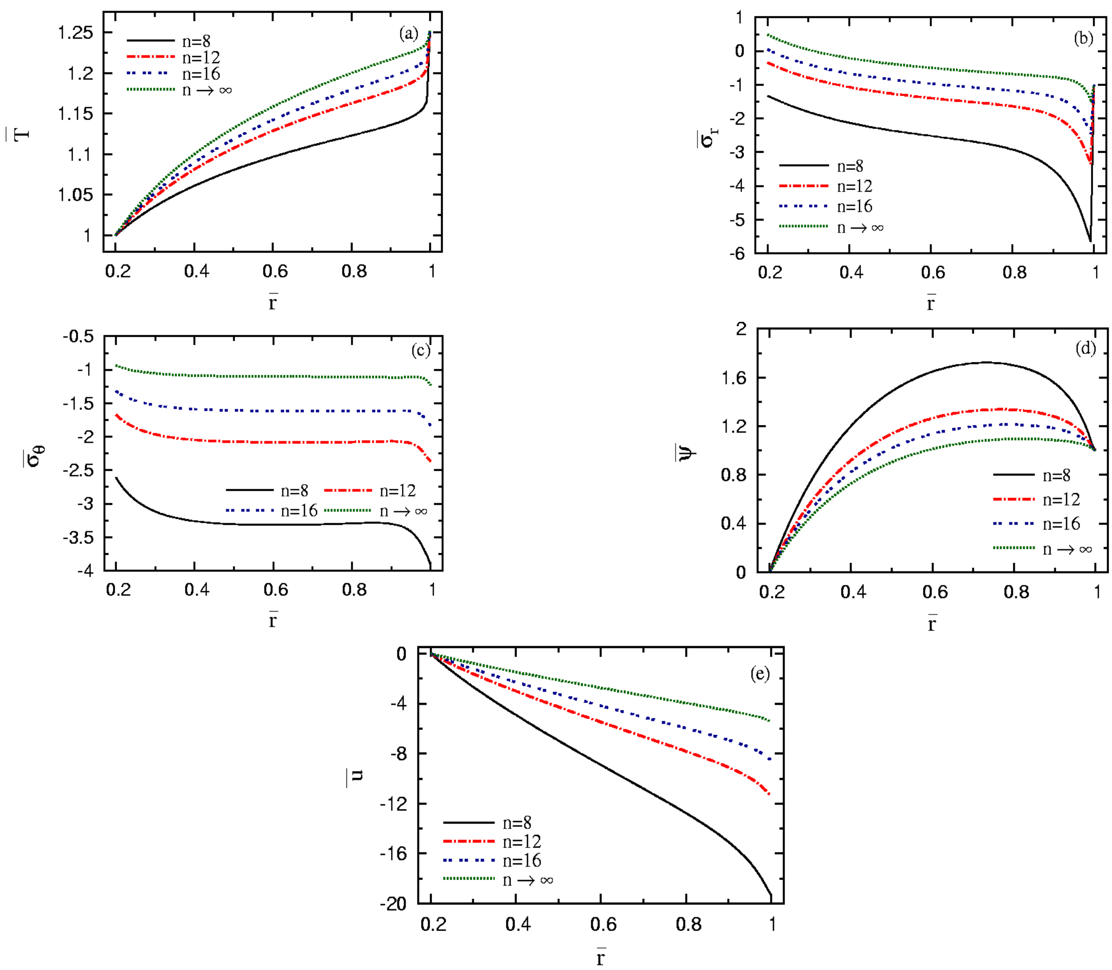

Fig. 9. Influence of grading index in even porosity distribution on mounted hollow FG cylinder and electrical loading.

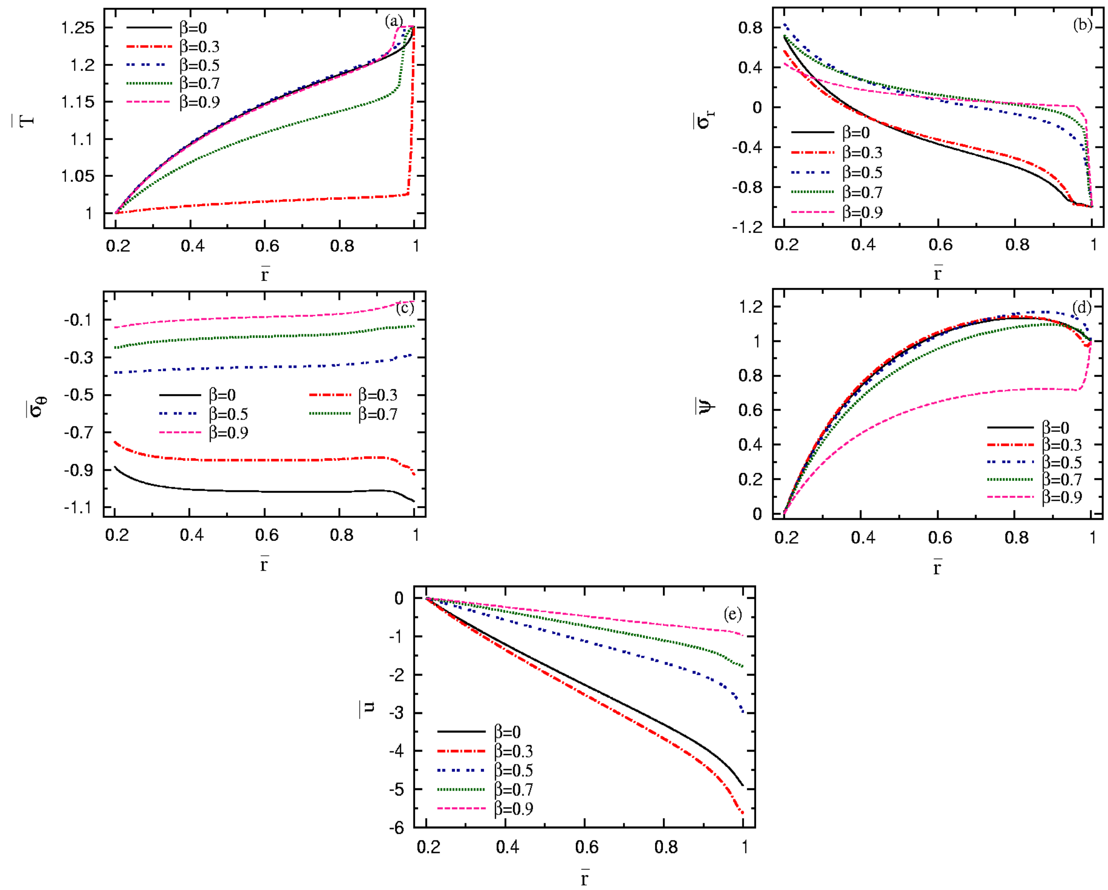

Fig. 10. Effectiveness of porosity parameter in even porosity distribution on mounted hollow FG cylinder and electrical loading.

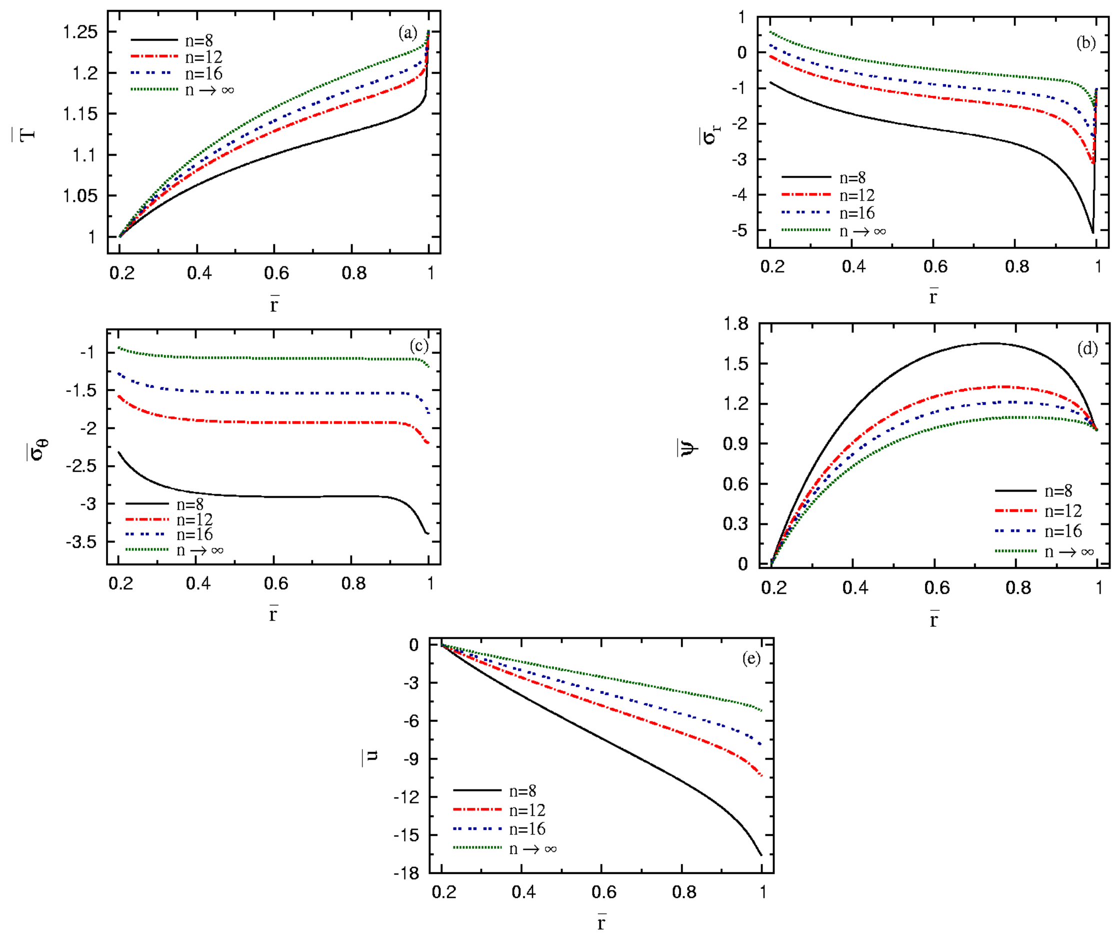

Fig. 11. Influence of grading index in uneven I porosity distribution on mounted hollow FG cylinder and electrical loading.

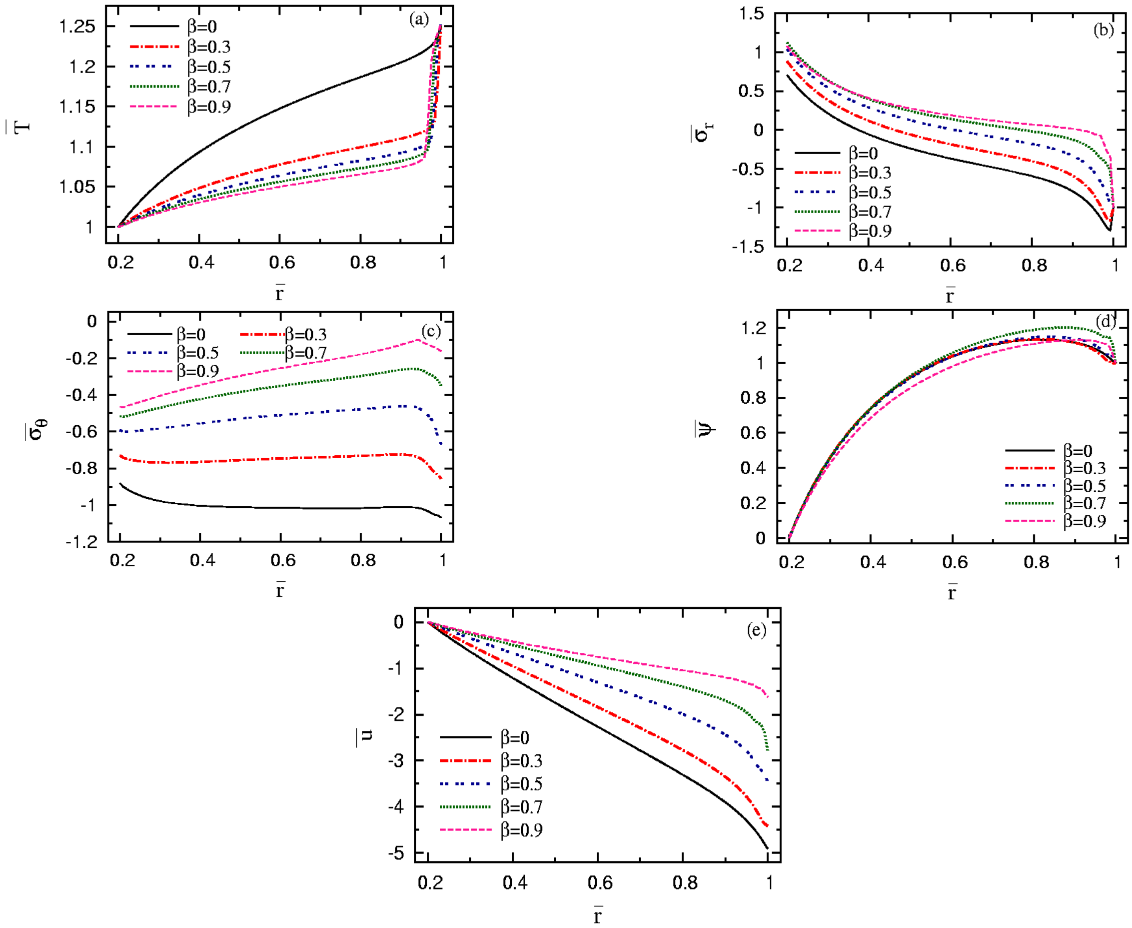

Fig. 12. Effectiveness of porosity parameter in uneven I porosity distribution on mounted hollow FG cylinder and electrical loading.

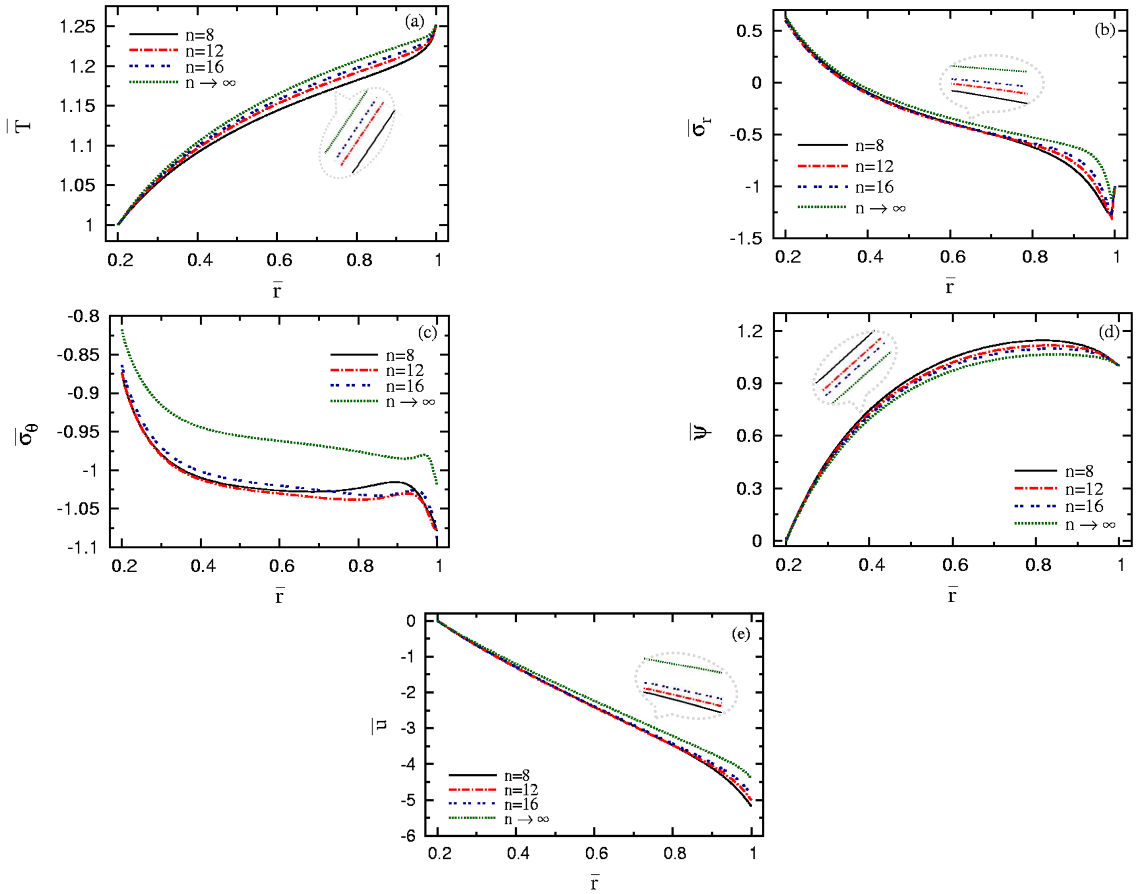

Fig. 13. Influence of grading index in uneven II porosity distribution on mounted hollow FG cylinder and electrical loading.

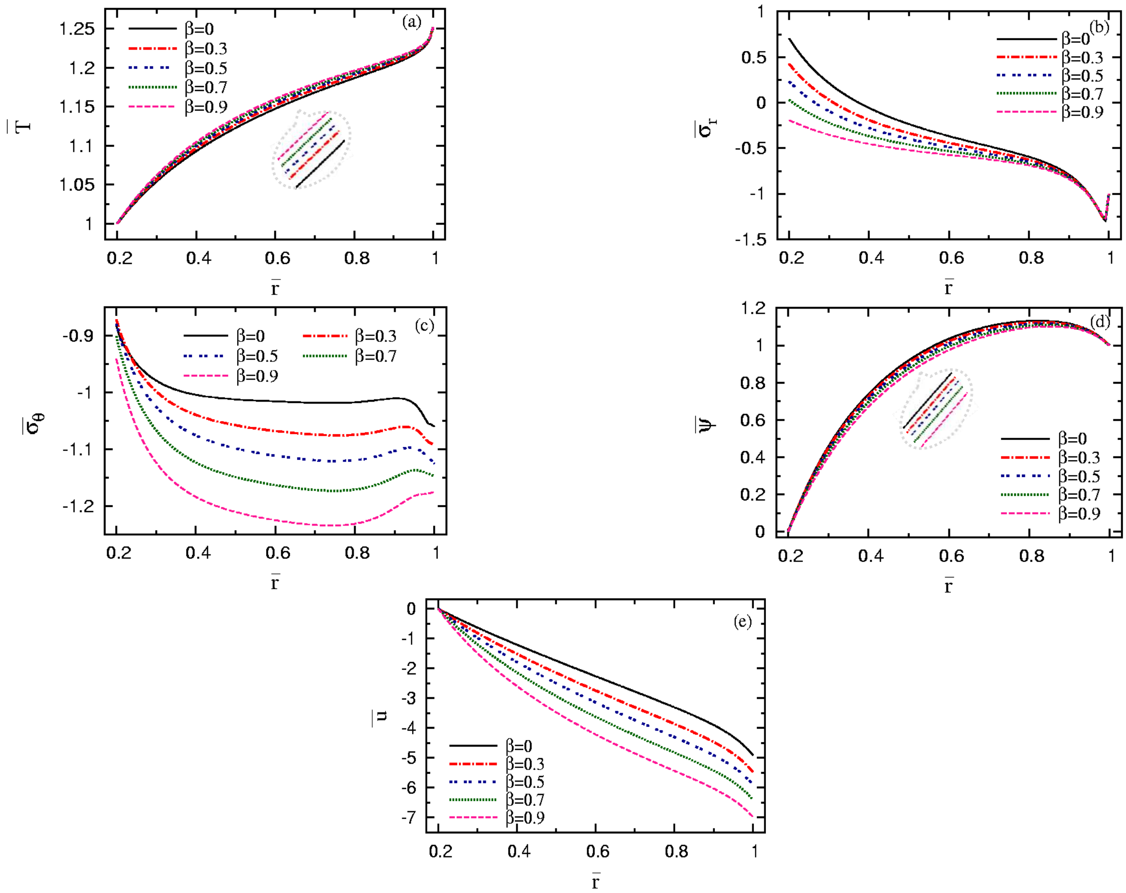

Fig. 14. Effectiveness of porosity parameter in uneven II porosity distribution on mounted hollow FG cylinder and electrical loading.

Figure 13 is presented to survey uneven II logarithmic distribution 2 and its relationship to the gradient coefficient n. Among them Fig.13a with temperature curves $\bar{T}$, Fig. 13b with radial stress curves $\bar{\sigma}_\theta$, and Fig.13e with radial displacement $\bar{u}$. They form a direct relationship with the gradient coefficient n, meaning that the greater the value of gradient index n, the greater the value of curves. As for the hoop stress $\bar{\sigma}_\theta$, it was presented in Fig.13c, where it appears that the lowest value of hoop stress $\bar{\sigma}_\theta$ is at $n = 12$ and the highest value of hoop stress $\bar{\sigma}_\theta$ is at $n \longrightarrow \infty$. The electrical potential $\bar{\psi}$ is presented in Fig. 13d. It achieved an inverse relationship between the electrical potential $\bar{\psi}$ and the gradient coefficient n. The greater the value of gradient factor n, the lower the value of electrical potential $\bar{\psi}$.

The second part of the study of uneven II logarithmic distribution is presented in Fig. 14. It is clear from it that all of the cylinder parameters achieved an inverse relationship with the porosity coefficient β, except for the temperature curves $\bar{T}$ in Fig. 14a, which achieved a direct relationship with the porosity coefficient β.

9. Conclusions

The current study examined three different types of irregular porosity distributions on a hollow FG cylinder rotating around a fixed axis and placed within a stable magnetic field. The study was carried out under thermal and mechanical forces. The three distributions were an even distribution, an uneven I logarithmic distribution, and an uneven II logarithmic distribution. The resulting system of differential equations was solved using the semi-analytical method for two boundary conditions, (free-free) mechanical pressure and electrical loading and (fixed-free) mounted hollow porous cylinder. A comparison was made between numerical outcomes in two statuses with variation in the gradient factor and the porosity coefficient, and we obtained the following results:

- Values of temperature, stress, and electrical potential are greatly affected by differences in gradient factor and porosity coefficient.
- Results of even distribution of porosity converge in the results with the results of non-porous cylinder.
- Numerical outcomes in the status of uneven logarithmic distribution I and II were monitored in Tables 2 and 3, and a large difference appeared in the numerical results between the two distributions.
- Through the results, it is possible to choose appropriate values for the gradient factor and the porosity coefficient to obtain specific values for the stresses and displacements in a porous cylinder for each distribution separately.
- The study is very important in designing a composite model of a porous cylinder with graduated properties under the influence of different forces and obtaining specific results in modern engineering designs.

Author Contributions

The authors participated in choosing the research idea, programming, and discussing the results together. The manuscript was written through the contribution of all authors. All authors discussed the results, reviewed, and approved the final version of the manuscript.

Acknowledgments

Not applicable.

Conflict of Interest

The authors confirm the integrity of the research without any scientific or financial problems.

Funding

The authors received no financial support for the research, authorship, and publication of this article.

Data Availability Statements

All scientific data used in the research are available for scientific research through the authors.

Nomenclature

a	Interior cylinder radius $[\mathrm{m}]$	$\alpha_i\ (i=r,\theta)$	Thermal expansion coefficients $[\mathrm{K}^{-1}]$
b	Exterior cylinder radius $[\mathrm{m}]$	β	Porosity factor
c_{ij}	Elastic coefficients $[\mathrm{Pa}]$	D_r	Electric displacement
$e_{rj}\ (j=r,\theta)$	Piezoelectric coefficients $[\mathrm{C\ m}^{-2}]$	ε_{rr}	Dielectric coefficients $[\mathrm{C}^2\mathrm{K}^{-1}\mathrm{m}^2]$
H	Static magnetic medium $[\mathrm{kg\ C}^{-1}\ \mathrm{sec}^{-1}]$	ψ	Electric potential distribution $[\mathrm{W/A}]$
K_T	Thermal conductivity coefficient $[\mathrm{W/K\ m}]$	$\mu(r)$	Magnetic permeability $[\mathrm{Hm}^{-1}]$
n	Grading index	ω	Angular velocity
$r^{(k)}$	Average radii of a kth layer $[\mathrm{m}]$	$s^{(k)}$	The radial thickness of a kth layer $[\mathrm{m}]$
σ_r	Radial stress $[\mathrm{Pa}]$	σ_θ	Circumferential stress $[\mathrm{Pa}]$
$T(r)$	Temperature distribution $[\mathrm{K}]$	T_0	Initial temperature $[\mathrm{K}]$
ρ	Density $[\mathrm{kg\ m}^{-3}]$	p_a	Property of an interior surface
p_b	Property of the exterior surface	p_{11}	Pyroelectric parameters $[\mathrm{CK}^{-1}\mathrm{m}^{-2}]$
P_1	Interior pressure $[\mathrm{Pa}]$	P_2	Exterior pressure $[\mathrm{Pa}]$
$u(r)$	Radial displacement $[\mathrm{m}]$		

References

[1] Xu, Q., Ma, A., Saleh, B., Li, Y., Yuan, Y., Jiang, J., Ni, C., Enhancement of strength and ductility of SiCp/AZ91 composites by RD-ECAP processing, *Materials Science and Engineering: A*, 771, 2019, 138579.
[2] Li, W., Han, B., Research and application of functionally gradient materials, *IOP Conference Series: Materials Science and Engineering*, 394, 2018, 1–7.
[3] Saleh, B., Jiang, J., Ma, A., Song, D., Yang, D., Xu, Q., Review on the influence of different reinforcements on the microstructure and wear behavior of functionally graded aluminum matrix composites by centrifugal casting, *Metals and Materials International*, 26, 2020, 933–960.
[4] Tarlochan, F., Functionally graded material: a new breed of engineered material, *Journal of Applied Mechanical Engineering*, 1(5), 2012, 1-5.
[5] J Xie, P Shi, F Li, Exact solutions for the symmetric elastoplastic response of functionally graded pressure vessels, *Thin-Walled Structures*, 192, 2023, 111165.
[6] Saadatfar, M., Zarandi, M.H., Effect of angular acceleration on the mechanical behavior of an exponentially graded piezoelectric rotating annular plate with variable thickness, *Mechanics Based Design of Structures and Machines*, 50(4), 2022, 1354–1370.
[7] Allam, M.N.M, Zenkour, A.M., Tantawy, R., Analysis of functionally graded piezoelectric cylinders in a hygrothermal environment, *Advances in Applied Mathematics and Mechanics*, 6(2), 2014, 233-246.
[8] Allam, M.N.M., Tantawy, R., Zenkour, A.M., Magneto-thermo-elastic response of exponentially graded piezoelectric hollow spheres, *Advances in Computational Design*, 3(3), 2018, 303-318.
[9] Thanh, T.T., Ke, T.V., Hoa, P.Q., Van, T.T., Trung, N.T., An edge-based smoothed finite element for buckling analysis of functionally graded material variable thickness plates, *Vietnam Journal of Mechanics*, VAST, 43(3), 2021, 221–235.
[10] Saadatfar, M., Zarandi, M.H., Effect of angular acceleration on the mechanical behavior of an exponentially graded piezoelectric rotating annular plate with variable thickness, *Mechanics Based Design of Structures and Machines*, 50(4), 2022, 1354-1370.
[11] Sharma, D., Kaur, R., Sharma, H., Investigation of thermo-elastic characteristics in functionally graded rotating disk using finite element method, *Nonlinear Engineering*, 10(1), 2021, DOI: 10.1515/nleng-2021-0025.
[12] Chen, D., Yang, J., Kitipornchai, S., Elastic buckling and static bending of shear deformable functionally graded porous beam, *Composite Structures*, 133, 2015, 54–61.
[13] Kitipornchai, S., Chen, D., Yang, J., Free vibration and elastic buckling of functionally graded porous beams reinforced by graphene platelets, *Materials and Design*, 116, 2017, 656–665.
[14] Wang, Y., Zhang, L., Daynes, S., Zhang, H., Feih, S., Wang, M.Y., Design of graded lattice structure with optimized mesostructures for additive manufacturing, *Materials and Design*, 142, 2018, 114–123.
[15] Nazir, A., Jeng, J.Y., Buckling behavior of additively manufactured cellular columns: experimental and simulation validation, *Materials and Design*, 186, 2020, 108349.
[16] Tantawy, R., Zenkour, A.M., Effect of Porosity and Hygrothermal Environment on FGP Hollow Spheres under Electromechanical Loads, *Journal of Applied and Computational Mechanics*, 8(2), 2022, 710–722.
[17] Wattanasakulpong, N., Ungbhakorn, V., Linear and nonlinear vibration analysis of elastically restrained ends FGM beams with porosities, *Aerospace Science and Technology*, 32(1), 2014, 111–120.
[18] Tantawy, R., Magneto-electric influence on a functionally graded porous hollow structure in hygrothermal environment, *Scientific Journal for Damietta Faculty of Science*, 12 (1), 2022, 1-15.
[19] Babaei, M., Kiarasi, F., Asemi, K., Hosseini, M., Functionally graded saturated porous structures: A review, *Journal of Computational Applied Mechanics*, 53(2), 2022, 297-308.
[20] Nathi, V. K., Buckling analysis of 2D functionally graded porous beams using novel higher order theory, *Journal of Computational Applied Mechanics*, 53(3), 2022, 393-413.
[21] Tantawy, R. M., Zenkour, A. M., Bending Response of a Rotating Viscoelastic Functionally Graded Porous Disk with Variable Thickness, *Journal of Computational Applied Mechanics*, 54(4), 2023, 482-500.
[22] Li, X., Wang, T., Liu, F., Zhu, Z., Computer simulation of the nonlinear static behavior of axially functionally graded microtube with porosity, *Advances in Nano Research*, 11(4), 2021, 437–451.
[23] Li, C., Shen, H. S., Yang, J., Nonlinear Vibration Behavior of FG Sandwich Beams with Auxetic Porous Copper Core in Thermal Environments,

International Journal of Structural Stability and Dynamics, 2023, 2350144.
[24] Tantawy, R.M., Zenkour, A.M., Effects of porosity, rotation, thermomagnetic, and thickness variation on functionally graded tapered annular disks, *Information Sciences Letters*, 12(3), 2023, 1133–1150.
[25] Ebrahimi, F., Jafari, A., Barati, M.R., Vibration analysis of magneto-electro-elastic heterogeneous porous material plates resting on elastic foundations, *Thin-Walled Structures*, 119, 2017, 33–46.
[26] Akbas, S., Thermal Effects on the Vibration of Functionally Graded Deep Beams with Porosity, *International Journal of Applied Mechanics*, 9(5), 2017, 1750076.
[27] Tantawy, R., Zenkour, A.M., Even and uneven porosities on rotating functionally graded variable thickness annular disks with magneto-electro thermo-mechanical loadings, *Journal of Applied and Computational Mechanics*, 9(3), 2023, 695–711.
[28] Barati, M.R., Shahverdi, H., Aero-hygro-thermal stability analysis of higher-order refined supersonic FGM panels with even and uneven porosity distributions, *Journal of Fluids and Structures*, 73, 2017, 125–136.
[29] Ootao, Y., Tanigawa, Y., Transient piezothermoelastic analysis for a functionally graded thermopiezoelectric hollow sphere, *Composite Structures*, 81, 2007, 540–549.
[30] Arani, A.G., Kolahchi, R., Mosallaie Barzoki, A.A., Loghman, A., Electro-thermo-mechanical behaviors of FGPM spheres using analytical method and ANSYS software, *Applied Mathematical Modelling*, 36, 2012, 139–157.
[31] Vaka, V., Sathujoda, P., Bhalla, N.A., Kumar, Y.V.S., Steady-state and transient vibration analysis of a thermally loaded power law-based functionally graded rotor system with induced porosities, *Forces in Mechanics*, 9, 2022, 100123.
[32] Nikarad, S.F., Kanellopoulos, A., Bodaghi, M., Chen, Z.T., Large deformation behavior of functionally graded porous curved beams in thermal environment, *Archive of Applied Mechanics*, 91, 2021, 2255–2278.
[33] Bayat, M., Rahimi, M., Saleem, M., Mohazzab, A. H., Wudtke, I., Talebi, H., One dimensional analysis for magnetothermo- mechanical response in a functionally graded annular variable-thickness rotating disk, *Applied Mathematical Modelling*, 38(19), 2014, 4625–4639.
[34] Marin, M., Öchsner, A., Bhatti, M.M., Some results in Moore-Gibson-Thompson thermoelasticity of dipolar bodies, *ZAMM-Journal of Applied Mathematics and Mechanics*, 100(12), 2020, 1-13.
[35] Kraus, J.D., *Electromagnetic*, McGraw Hill. Inc., U.S.A., 1984.
[36] Dai, T., Dai, H.L., Analysis of a rotating FGMEE circular disk with variable thickness under thermal environment, *Applied Mathematical Modelling*, 45, 2017, 900–924.
[37] Dai, H.L., Jiang, H.J., Analytical study for electromagnetothermoelastic behavior of a functionally graded piezoelectric solid cylinder, *Mechanics of Advanced Materials and Structures*, 20(10), 2013, 800–811.
[38] Marin, M., Agarwal, R.P., Mahmoud, S.R., Modeling a microstretch thermo-elastic body with two temperatures, *Abstract and Applied Analysis*, 2013, 2013, 1-7.
[39] Vlase, S., Nastac, C., Marin, M., Mihalcica, M., A method for the study of the vibration of mechanical bars systems with symmetries, *ACTA Technica Napocensis - Series: Applied Mathematics, Mechanics, And Engineering*, 60(4), 2017, 539-544.
[40] Mendelson, A., *Plasticity Theory and Applications*, Macmillan, New York, 1968.

ORCID iD

Rania M. Tantawy https://orcid.org/0000-0002-0576-2798
Mohammed A. Alghamdi https://orcid.org/0000-0002-4162-4966
Ashraf M. Zenkour https://orcid.org/0000-0002-0883-8073

How to cite this article: Tantawy, R.M., Alghamdi, M.A., Zenkour, A.M. Non-uniform porosity distribution on a hollow cylinder with thermo-magnetic mechanical loading, *J. Appl. Comput. Mech.*, 11(4), 2025, 975-990.
https://doi.org/10.22055/jacm.2024.47920.4842